Charge Collection and Space Charge Distribution in Neutron-Irradiated Epitaxial Silicon Detectors

Diplomarbeit
von
Thomas Pöhlsen

Universität Hamburg
Institut für Experimentalphysik

April 2010

Charge Collection and Space Charge Distribution in Neutron-Irradiated Epitaxial Silicon Detectors
-
Ladungssammlung und Raumladungsverteilung in neutronenbestrahlten epitaktischen Siliziumdetektoren

Diplomarbeit
eingereicht von

Thomas Pöhlsen

Matrikelnummer: 5725201

Universität Hamburg
Fachbereich Physik
Institut für Experimentalphysik

Erstgutachter: Prof. Dr. Robert Klanner
Zweitgutachterin: Prof. Dr. Caren Hagner

Abstract

In this work epitaxial n-type silicon diodes with a thickness of 100 μm and 150 μm are investigated.

After neutron irradiation with fluences between 10^{14} cm^{-2} and 4×10^{15} cm^{-2} annealing studies were performed. CV-IV curves were taken and the depletion voltage was determined for different annealing times. All investigated diodes with neutron fluences greater than 2×10^{14} cm^{-2} showed type inversion due to irradiation.

Measurements with the transient current technique (TCT) using a pulsed laser were performed to investigate charge collection effects for temperatures of −40°C, −10°C and 20°C. The charge correction method was used to determine the effective trapping time τ_{eff}. Inconsistencies of the results could be explained by assuming field dependent trapping times. A simulation of charge collection could be used to determine the field dependent trapping time $\tau_{eff}(E)$ and the space charge distribution in the detector bulk. Assuming a linear field dependence of the trapping times and a linear space charge distribution the data could be described.

Indications of charge multiplication were seen in the irradiated 100 μm thick diodes for all investigated fluences at voltages above 800 V.

The space charge distribution extracted from TCT measurements was compared to the results of the CV measurements and showed good agreement.

Zusammenfassung

Im Rahmen dieser Diplomarbeit wurden epitaktische n-Typ Siliziumdetektoren mit Dicken von 100 μm und 150 μm untersucht.

Nach Neutronenbestrahlung mit Fluenzen von 10^{14} cm^{-2} bis 4×10^{15} cm^{-2} wurden Ausheilstudien durchgeführt. Die CV/IV-Kurven wurden für verschiedene Ausheilzeiten aufgenommen und die zugehörigen Verarmungsspannungen bestimmt. Alle untersuchte Dioden mit Fluenzen über 2×10^{14} cm^{-2} zeigten Typeninversion aufgrund der Bestrahlung.

Messungen mit der Transient Current Technique (TCT) wurden mit einem gepulsten Laser durchgeführt, um Ladungssammlungseffekte für Temperaturen von −40°C, −10°C und 20°C zu untersuchen. Die Charge Correction Method wurde benutzt, um die effektive Einfangzeit τ_{eff} zu bestimmen. Inkonsistenzen der Messergebnisse konnten durch feldabhängigen Elektroneneinfang erklärt werden. Eine Simulation der Ladungssammlung wurde benutzt um die feldabhängige Einfangzeit $\tau_{eff}(E)$ und die Raumladungsverteilung im Diodeninneren zu bestimmen. Unter der Annahme einer linear feldabhängigen Einfangzeit und einer linearen Raumladungsverteilung konnten die Messdaten gut beschrieben werden.

Anzeichen von Ladungsvervielfachung in den bestrahlten, 100 μm dicken Dioden wurden für alle untersuchten Fluenzen bei Spannungen über 800 V festgestellt.

Die aus den TCT-Messungen gewonnene Raumladungsverteilung wurde mit den Ergebnissen der CV-Messungen verglichen und zeigt gute Übereinstimmung.

Contents

1 Introduction **1**

2 Silicon Diodes **3**
2.1 Production Methods of Silicon Crystals 3
2.2 Electrical Properties of Silicon Diodes 4
2.2.1 p-n Junction and Electric Field 4
2.2.2 CV-IV Characteristics 6
2.3 Charge Collection 8
2.3.1 Drift Velocity 8
2.3.2 Charge Collection Efficiency 10
2.3.3 Charge Multiplication 10
2.4 Radiation Damage 11
2.4.1 Different Radiation Types and Equivalent Fluence 11
2.4.2 Defect Kinetics and Annealing 13
2.4.3 Depletion Voltage and Type Inversion 13
2.4.4 Trapping and Charge Collection Efficiency 13
2.4.5 Reverse Current 14
2.4.6 Inhomogeneous Space Charge Distribution 15

3 Experimental Setup **17**
3.1 Investigated Samples and Irradiation 17
3.1.1 Material 17
3.1.2 Structure 17
3.1.3 Irradiation 18
3.2 CV-IV Measurements 18
3.2.1 CV Measurements 19
3.2.2 IV Measurements 19
3.3 Transient Current Technique (TCT) 19
3.3.1 The Different TCT Setups 20
3.3.2 Laser Output Power Stability 21
3.3.3 Determination of the Collected Charge Q 22
3.3.4 Determination of the Charge Collection Efficiency 24
3.3.5 Charge Carrier Density Effects 24

4 Analysis **27**
4.1 CV Measurements 27
4.1.1 Determination of the Diode Thickness 27
4.1.2 Determination of the Depletion Voltage 27

4.1.3 Determination and Description of the Space Charge . . . 29
4.2 Charge Correction Method . . . 30
4.2.1 Assumptions . . . 30
4.2.2 Compensation of Trapping . . . 31
4.2.3 Data Preparation . . . 32
4.3 Simulation of Charge Collection for Unirradiated Diodes . . . 36
4.3.1 Assumptions . . . 36
4.3.2 Circuit Simulation . . . 37
4.3.3 Deposited Charge Q_0 . . . 38
4.4 Simulation of Charge Collection for Irradiated Diodes . . . 38
4.4.1 Assumptions . . . 39
4.4.2 Deposited Charge Q_0 . . . 40
4.4.3 Determination of Trapping Time by a CCE Fit . . . 40
4.4.4 Determination of the Space Charge Distribution . . . 42

5 Results and Discussion **47**
5.1 CV-IV Measurements . . . 47
5.1.1 Annealing Studies and Type Inversion . . . 47
5.1.2 Depletion Voltage and Space Charge Distribution . . . 49
5.1.3 Radiation Induced Reverse Current I_{dep} . . . 49
5.2 Charge Correction Method . . . 51
5.2.1 Voltage Range for the Zero-Slope Condition . . . 51
5.2.2 Field Dependent Trapping as a Reason for Voltage Dependency . . . 51
5.2.3 Charge Carrier Density Effects . . . 53
5.2.4 Time Resolution . . . 53
5.3 Simulation of Charge Collection . . . 53
5.3.1 Space Charge Distribution . . . 53
5.3.2 Trapping Time . . . 59
5.3.3 Charge Multiplication . . . 62

6 Summary and Conclusion **65**

List of Figures **67**

List of Tables **69**

Bibliography **71**

Chapter 1

Introduction

At the Large Hadron Collider (LHC) at CERN in Geneva proton-proton-interactions at a centre of mass energy of 14 TeV and a luminosity of 10^{34} cm^{-2}s^{-1} will be investigated. These interactions will be studied in four different experiments: ATLAS, ALICE, CMS and LHCB. The tracker is the inner component of these experiments close to the interaction point. It is used to trace the trajectories of the outgoing charged particles produced in the collision.

Close to the interaction point the tracker is built of silicon pixel detectors. Due to the high particle fluences in this region the pixel detectors are irradiated strongly and radiation damage occurs. Higher voltage is needed for full depletion and the leakage current increases, which leads to higher noise and power consumption. Furthermore the irradiation defects cause trapping of free charge carriers and the charge collection efficiency is reduced. Thus the signal to noise ratio is smaller than in unirradiated detectors.

For the LHC these defects require to replace the pixel detectors after 5 years of operation. After 10 years of operation the LHC is planned to be upgraded and will then be named Super Large Hadron Collider (SLHC). The SLHC will offer a luminosity increased by a factor of 10 up to 10^{35} cm^{-2}s^{-1} and thus will lead to a much higher irradiation of the used detectors. After 5 years of operation at SLHC luminosities the total fluence in the inner detectors will be in the order of 10^{16} cm^{-2} (compare Figure 1.1).

These higher fluences require the use of radiation hard detectors which are developed and investigated in different research programs. This work is done in the framework of the CERN Research and Development program RD50.

There are different approaches to increase the radiation hardness of silicon detectors: device engineering and defect engineering. In terms of device engineering it turned out that relatively thin diodes with a thickness of about 100 μm might be suitable to reach a good signal to noise ratio at high fluences. If the diodes are too thin noise will increase due to high capacitances and signal decreases since the deposited charge of the particles to be detected (MIPs) is proportional to diode thickness. If diodes are too thick trapping becomes more relevant because the charge collection time increases. Further the induced radiation defects will make it impossible to fully deplete the diodes. The sensitive volume will be reduced and

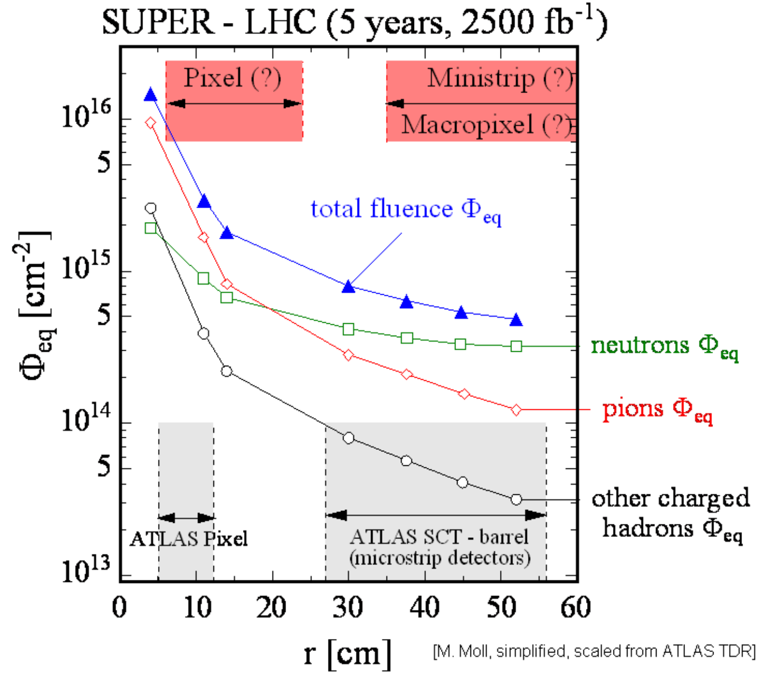

Figure 1.1: Super LHC equivalent fluences, normalised to 1 MeV neutrons. By [Mol99].

small electric fields close the depletion junction will further increase the charge collection time. In terms of defect engineering a high oxygen concentration inside the silicon is considered to be beneficial for radiation hardness [Cas09].

Since epitaxial silicon (EPI) offers both, a high oxygen concentration and the possibility to grow thin crystals, EPI diodes are good candidates to be used at SLHC fluences. In this work the effect of neutron irradiation on 100 µm and 150 µm thick n-type EPI-ST (standard oxygen concentration) and EPI-DO (oxygen enriched) diodes are investigated.

In this work we focus on the investigation of charge trapping and the change of effective doping due to irradiation. Trapping is considered to be the most limiting factor at SLHC fluences [Cas09]. The space charge leads to a non-uniform distribution of the electric field inside the detector and defines the voltage needed for full depletion. Further charge multiplication is possible if locally very high electric fields are present. This effect might be used to compensate trapping at SLHC fluences.

Chapter 2

Silicon Diodes

In this chapter the principles of silicon diodes most relevant for this work will be treated.

2.1 Production Methods of Silicon Crystals

There are three main growing techniques for silicon: Czochralski (Cz), Float Zone (FZ) and epitaxial (EPI).

For Czochralski material a monocrystalline seed crystal is placed on the surface of a silicon melt. The crystal is slowly drawn upwards while the melt is rotated. At the interface of the crystal and the melt the melt solidifies with the same crystal orientation as the seed. A high amount of impurities characterises the Czochralski material.

For Float Zone material again a monocrystalline seed is needed. It is brought in contact with polycrystalline silicon and the region around the contact is melted with a radio frequency field. The melted region is called Float Zone. The Float Zone is shifted so that the monocrystalline seed grows. Compared to Czochralski material less impurities occur.

For epitaxial material a single crystal substrate is used. On this substrate a thin epitaxial layer is grown which adopts the crystal orientation of the substrate. Thus the epitaxial layer is monocrystalline.

The material used in this work is epitaxial material produced by ITME[1] with the vapour phase epitaxy method (VPE). Sometimes this method is also called chemical vapour deposition (CVD). At temperatures around 1200 °C the following reaction is used to grow the epitaxial layer:

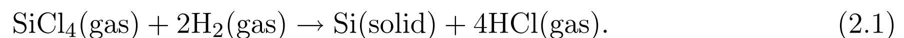

$$\mathrm{SiCl_4(gas)} + \mathrm{2H_2(gas)} \rightarrow \mathrm{Si(solid)} + \mathrm{4HCl(gas)}. \qquad (2.1)$$

By adding gases like diborane (B_2H_6) or phosphine (PH_3) p-type and n-type material can be produced, respectively.

As substrate highly doped Czochralski material is used so that the resistance of the substrate can be neglected and the sensitive region is limited to the epitaxial layer.

[1] Institute of Electronic Materials Technology (ITME), Warsaw, Poland.

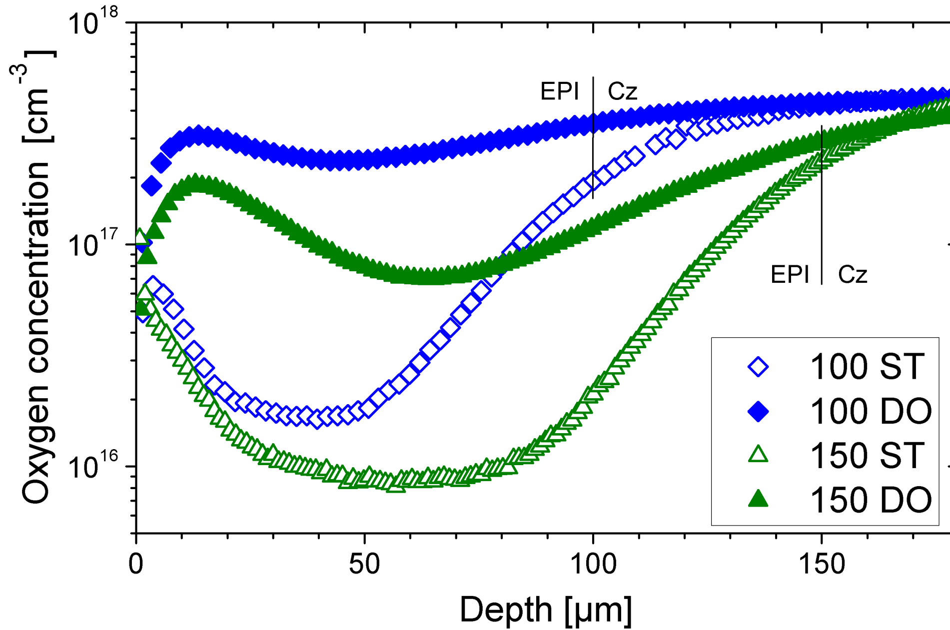

Figure 2.1: Oxygen concentration depth profile in 100 µm and 150 µm EPI diodes. Measurements were performed by SIMS and illustrated by [Lan08].

The high amount of impurities in Cz material can partly diffuse into the EPI layer. Especially oxygen has a high diffusion constant which naturally causes a high oxygen concentration in EPI material. The diffusion of oxygen can be further stimulated at temperatures of about 1100 °C. This leads to a higher and more homogeneous oxygen concentration as seen in Figure 2.1[2]. EPI material produced with stimulated diffusion is called diffusion oxygenated material (EPI-DO). Otherwise we have standard EPI material (EPI-ST).

The growing of the epitaxial layer usually takes about 1 min/µm. The thickest epitaxial layers available so far have a thickness of 150 µm.

2.2 Electrical Properties of Silicon Diodes

2.2.1 p-n Junction and Electric Field

The band structure of semiconductors is characterised by the energy gap between valence band and conduction band. For intrinsic (pure) silicon the energy gap is approximately 1.12 eV. The silicon can be doped by replacing some of the silicon atoms by either donors (n-type silicon) or by acceptors (p-type silicon). Donors have five valence electrons. Four of these electrons will form the covalent bonding to the neighbouring silicon atoms while the fifth electron is only loosely bound (∼ 45 meV ionisation energy for Si doped with phosphine). In the energy band the donor with its electron corresponds to a filled state close to the conduction band

[2]The measurements of the oxygen concentration were performed by the SIMS laboratory of the Physics Institute of the Polish Academy of Science, Warsaw, Poland.

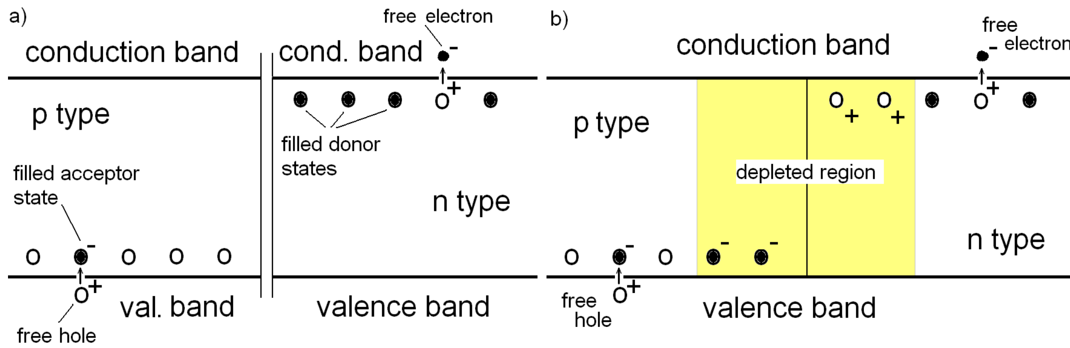

Figure 2.2: The p-n junction.

(see Figure 2.2 a). Its electron can be easily excited into the conduction band producing a free electron. At room temperature nearly all donor electrons will be excited. Acceptors have only three valence electrons and can accept a fourth electron. There energy level is close to the valence band. At room temperature most of the acceptors are filled with electrons from the valence band leading to free holes.

If n-type silicon and p-type silicon are joined together free electrons of the n-type silicon will diffuse into the p-type silicon and will recombine with holes there. In the same way free holes from the p-type region will diffuse into the n-type silicon and recombine with electrons there. This process will lead to a negative space charge at the filled acceptor states in the p-type silicon and to a positive space charge at the free donor states in the n-type silicon as indicated in Figure 2.2 b).

Due to the space charge close to the p-n junction an electric field is created. According to Gauss' law we have

$$\nabla E = \frac{\rho}{\epsilon\epsilon_0}, \tag{2.2}$$

with the space charge per unit volume ρ and $\epsilon = 11.9$ for silicon. The electric field will lead to a drift current of the free charge carriers opposing the diffusion of electrons and holes and eventually equilibrium is reached.

The space without free charge carriers is called depleted and its space charge density ρ in units of elementary charge q_0 is the same at the effective doping concentration[3] N_{eff}. For homogeneous doping and an abrupt p-n junction we have linear electric fields with a slope proportional to the doping concentration (see Equation 2.2). If no bias voltage is applied, the integral on the electric fields is called build in voltage U_{bi}. If we apply a bias voltage we change the electric field integral and we are able to decrease or increase the depletion width. For an abrupt p-n junction and partially depleted diodes with an applied reverse bias voltage U the depletion width $W(U)$ is given by

$$W(U) = \sqrt{\frac{2\epsilon\epsilon_0(U + U_{bi})}{q_0|N_{eff}|}}. \tag{2.3}$$

[3] The effective doping concentration N_{eff} is the difference of donor concentration and acceptor concentration

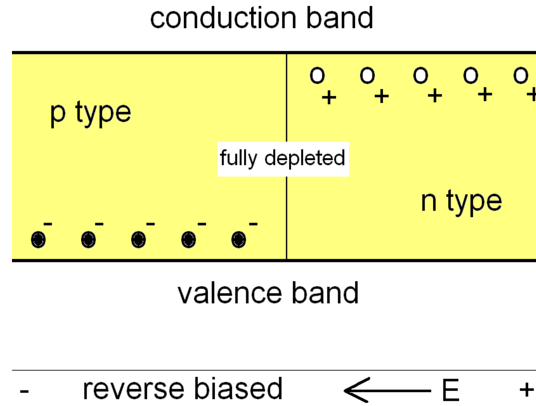

Figure 2.3: Fully depleted p-n junction.

Usually we will apply voltages large compared to $U_{bi} \approx 0.5$ V and we may simplify the depletion width to

$$W(U) = \sqrt{\frac{2\epsilon\epsilon_0 U}{q_0|N_{eff}|}}. \tag{2.4}$$

The voltage needed for full depletion of a diode with thickness d is called depletion voltage U_{dep} and can be calculated from Equation 2.4:

$$U_{dep} = \frac{d^2 q_0|N_{eff}|}{2\epsilon\epsilon_0} \tag{2.5}$$

For $U \geq U_{dep}$ the diode is fully depleted (see Figure 2.3) and the depletion width is equal to the diode thickness: $W(U) = d$.

2.2.2 CV-IV Characteristics

In this section the capacitance-voltage (CV) and the current-voltage (IV) characteristics for unirradiated planar silicon diodes will be discussed. Figure 2.4 shows the CV curve and the IV curve for an unirradiated diode.

Capacitance

For unirradiated diodes with thickness d, area A and depletion width $W(U)$ the capacitance is given by

$$C = \frac{dQ}{dU} = \epsilon\epsilon_0 \frac{A}{W(U)} \tag{2.6}$$

For partially depleted diodes the depletion width $W(U)$ is given by Equation 2.4. For fully depleted diodes ($U \geq U_{dep}$) we have constant capacitance with

$$C = C_{end} = \epsilon\epsilon_0 \frac{A}{d}. \tag{2.7}$$

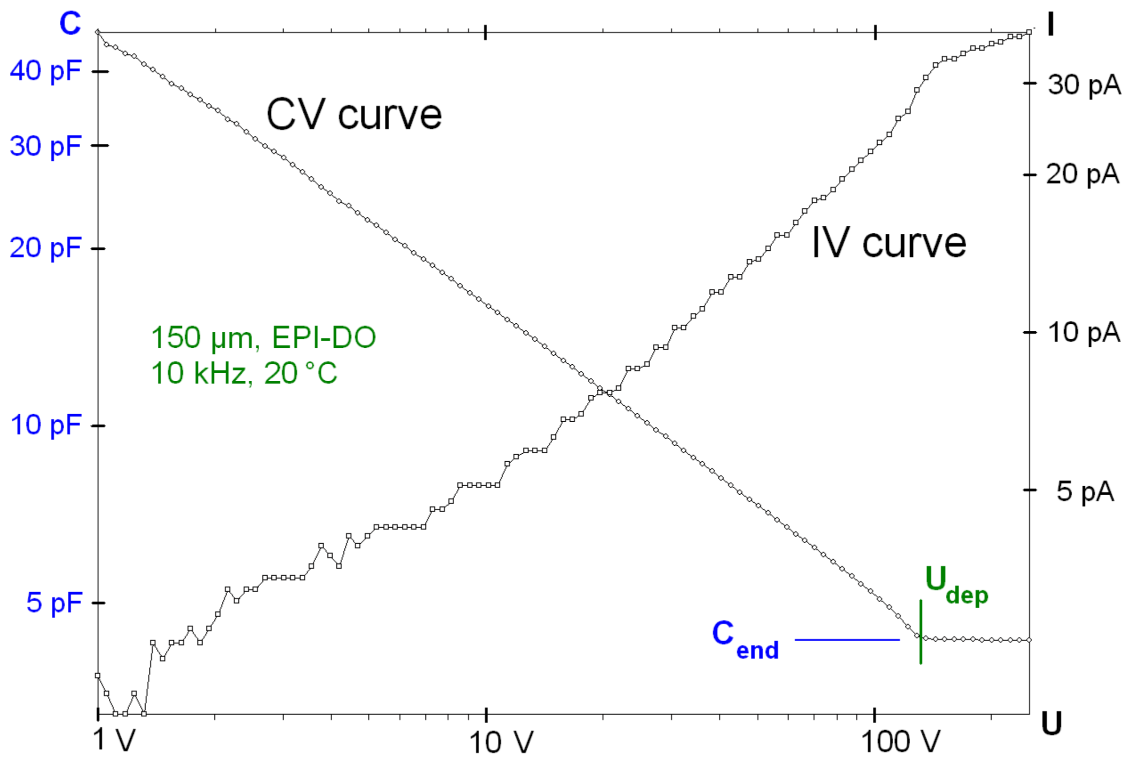

Figure 2.4: CV and IV curve for an unirradiated EPI-DO diode with a thickness of 150 µm, measured at 20 °C with 10 kHz frequency.

Diode Thickness

The thickness of a diode can be determined from the saturation capacitance C_{end} before irradiation, if the area of the depleted region is known.

Reverse Current

Electron-hole pairs are thermally generated at defects close to the middle of the band gap. If the electron-hole pairs are generated in the depleted region they contribute to the reverse current. Otherwise most of them will recombine. A first order approximation would be that the reverse current generated in the silicon bulk I_{bulk} (we neglect surface current here) is proportional to the depletion depth $W(U)$. Under this assumption we expect a saturation of I_{bulk} for fully depleted diodes.

The measured IV curve seen in Figure 2.4 shows a similar behaviour. Nevertheless, I_{bulk} does not saturate completely but still increases for voltages above full depletion. This behaviour might be explained by higher generation rates or by less recombination at high electric fields.

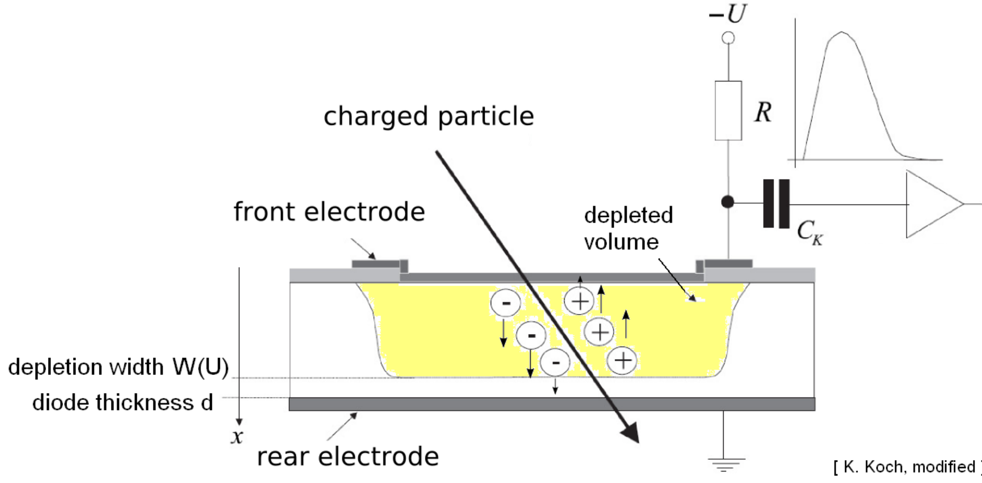

Figure 2.5: Principle of a silicon detector with thickness d and depletion width $W(U)$. The detector is sensitive in the depleted volume (yellow).

2.3 Charge Collection

Silicon diodes can be used to detect charged particles as shown in Figure 2.5. For the measurements of this work we use 100 µm and 150 µm thick planar epitaxial pad diodes. According to Ramo's theorem the induced current of N charge carriers (either holes or electrons) of charge q_0 in a fully depleted diode is given by

$$I(t) = \frac{q_0 N(t)}{d} v_{dr}(t), \tag{2.8}$$

with the drift velocity v_{dr} and the thickness of the diode d. If the number of drifting particles N is constant, i.e. there is no loss and no further generation of drifting particles, the collected charge Q is

$$Q = \int I(t)\mathrm{d}t = \frac{q_0 N}{d} \int \frac{\mathrm{d}x}{\mathrm{d}t} dt = q_0 N = Q_0. \tag{2.9}$$

In this case the collected charge is equal to the deposited charge Q_0.

2.3.1 Drift Velocity

The drift velocity v_{dr} is an implicit function of the time and should be written more precisely as $v_{dr}(E(x(t)))$, with $E(x(t))$ being the electric field at the position of the charge carrier x. Since v_{dr} is given by $\frac{dx}{dt}$, $t(x)$ can be written as

$$t(x) = \int_{x_0}^{x} \frac{1}{v_{dr}(E(x'))} dx', \tag{2.10}$$

with $x_0 = x(t = 0)$, the position where the charge carrier is created.

In this work we use the parameterisation of the drift velocity according to [Jac77]. Jacoboni

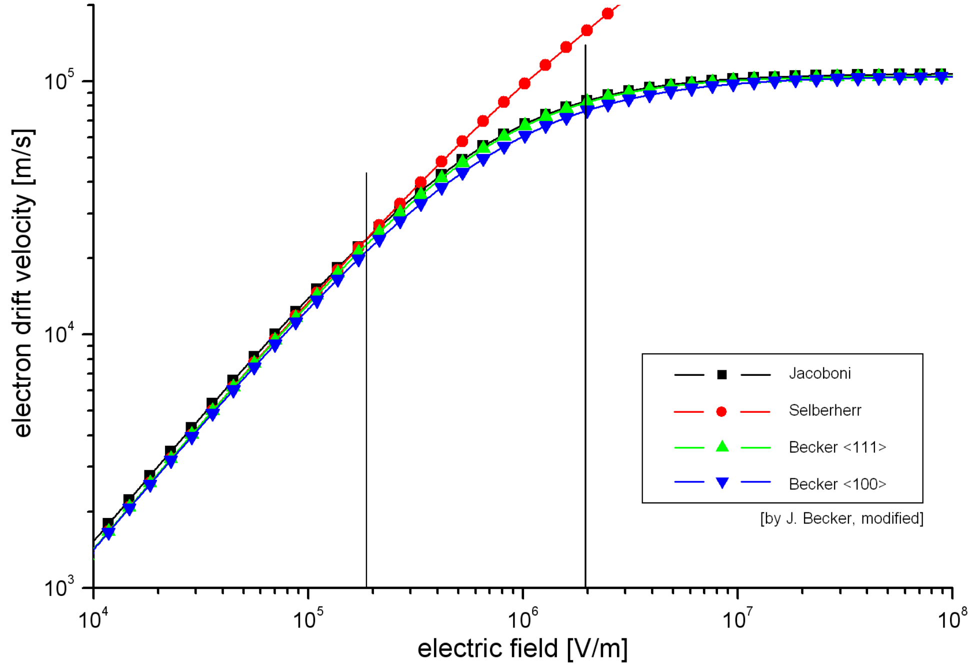

Figure 2.6: Anisotropy effects of the drift velocity of electrons at $T = 300$ K. The drift velocity fitted by [Bec10] for <100> and <111> direction is compared to the data according to [Jac77] and to [Sel00].

parameterised the drift velocity in <111> orientated silicon by

$$v_{dr} = \frac{\mu_0 E}{\left(1 + (\frac{\mu_0 E}{v_{sat}})^\beta\right)^{1/\beta}}, \tag{2.11}$$

with the low field mobility μ_0, the saturation velocity v_{sat} and the parameter β close to 1. All parameters, μ_0, v_{sat} and β are temperature dependent.

[Bec10] investigated anisotropy effects using the Jacoboni parameterisation and found values for the electron drift in <111> orientation in good agreement with [Jac77]. For electron drift in the <100> direction [Bec10] found different values leading to smaller drift velocities (compare Figure 2.6). For electrons and holes drifting in <100> direction the parameters by [Bec10] are given by following expression:

$$\begin{aligned}
\mu_{0,e} &= 1430\ \frac{cm^2}{Vs} && \cdot \left(\frac{T}{300\mathrm{K}}\right)^{-2.5} \\
v_{sat,e} &= 1.04 \cdot 10^7\ \frac{cm}{s} && \cdot \left(\frac{T}{300\mathrm{K}}\right)^{-0.85} \\
\beta_e &= 1.01 && \cdot \left(\frac{T}{300\mathrm{K}}\right)^{0.87} \\
\\
\mu_{0,h} &= 480\ \frac{cm^2}{Vs} && \cdot \left(\frac{T}{300\mathrm{K}}\right)^{-2.82} \\
v_{sat,h} &= 9.2 \cdot 10^6\ \frac{cm}{s} && \cdot \left(\frac{T}{300\mathrm{K}}\right)^{-0.04} \\
\beta_h &= 1.16 && \cdot \left(\frac{T}{300\mathrm{K}}\right)^{1.0}
\end{aligned} \tag{2.12}$$

Drift Velocity in Irradiated Silicon

In investigations of irradiated silicon up to fluences of $2.4 \cdot 10^{14}$ cm^{-2} performed by [Li95] and [Chi02] no significant change in saturation velocity and low field mobility could be found.

Diffusion

The thermal movement of free charge carriers leads to diffusion. The diffusion constant is given by $D = \mu kT/q_0$ leading to a spread of the charge carriers with time t of $\Delta x = \sqrt{2Dt}$[4]. The effect of diffusion may be neglected if the drift velocity v_{dr} is sufficiently large. In this case the spread of charge carriers in time $\Delta t = \Delta x / v_{dr}$ is small compared to the charge collection time t.

2.3.2 Charge Collection Efficiency

The charge collection efficiency (CCE) is the ratio of collected charge Q to the deposited charge Q_0

$$CCE = \frac{Q}{Q_0}. \tag{2.13}$$

As seen above for fully depleted unirradiated diodes the induced current integrated over time, Q, is equal to the deposited charge, Q_0 and the CCE is 1.

If some of the free charge carriers are lost, e.g. due to trapping (see Section 2.4), the collected charge Q will be smaller than the deposited charge Q_0 and CCE will be smaller than 1.

2.3.3 Charge Multiplication

Charge multiplication (sometimes also called avalanche effects) for high electric fields can cause the CCE to be greater than 1. Charge multiplication for N drifting electrons (or holes) can be described with the ionisation rate α by

$$\mathrm{d}N = \alpha N \mathrm{d}x \tag{2.14}$$

with the drift velocity v_{dr}.

According to [Gra73] electron multiplication in the electric field regime of less than $2 \cdot 10^5$ V/cm at room temperature can be described by the following expression:

$$\alpha = 2.6 \cdot 10^6 e^{-1.43 \cdot 10^6 / E} \tag{2.15}$$

with E in V cm^{-1} and α in cm^{-1}. We will neglect charge multiplication of holes in this electric

[4]We define Δx to be the distance between the point of maximum charge carrier concentration to the point where the charge carrier concentration is $1/e$ of the maximum charge carrier concentration.

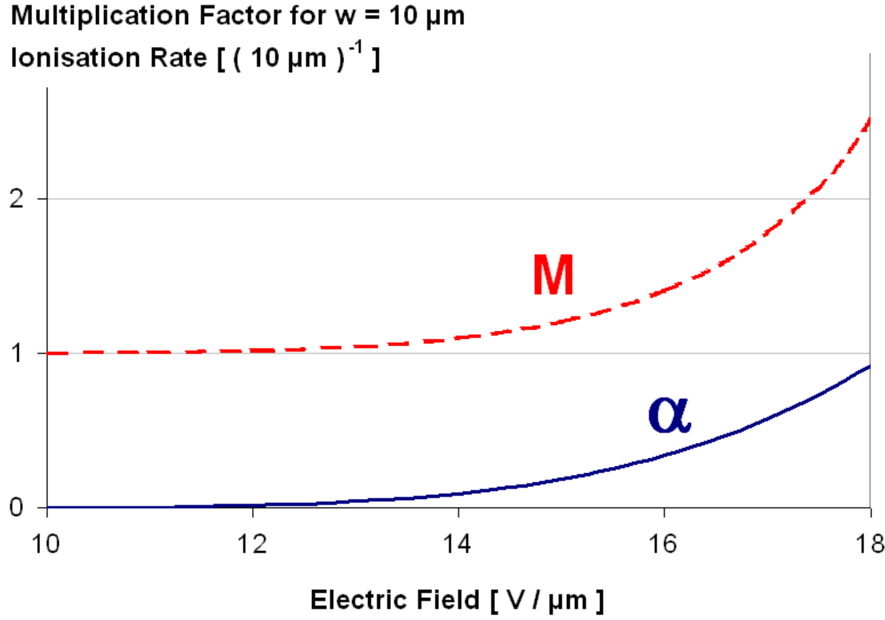

Figure 2.7: Ionisation rate α in (10 µm)$^{-1}$ and multiplication factor M for a 10 µm thick charge multiplication zone, versus electric field E.

field regime and obtain the charge multiplication factor for electrons

$$M = N/N_0 = e^{\int \alpha \, \mathrm{d}x}. \tag{2.16}$$

For the simple case of constant electric field E and a charge multiplication zone of width $w = 10$ µm we plotted M and α in Figure 2.7.

2.4 Radiation Damage

Particles crossing a silicon (Si) detector cause crystal defects which influence the detector performance. High energy particles can displace single or many Si atoms leaving vacancies (V) and Si interstitials (I) (Frenkel pairs). The energy loss, which results in displacement damage in the lattice, is called non-ionising energy loss (NIEL).

2.4.1 Different Radiation Types and Equivalent Fluence

The NIEL hypothesis states that changes in the material properties due to non-ionising energy loss are proportional to the energy imparted in displacing collisions. This assumption makes it possible to compare the displacement damage caused by different radiation types. Usually the radiation damage is compared with 1 MeV neutron radiation.

However, the probabilities that different defects are produced depends on the type of irradiation: for neutron irradiation a high number of cluster defects is seen, while for irradiation with charged hadrons there are more point defects.

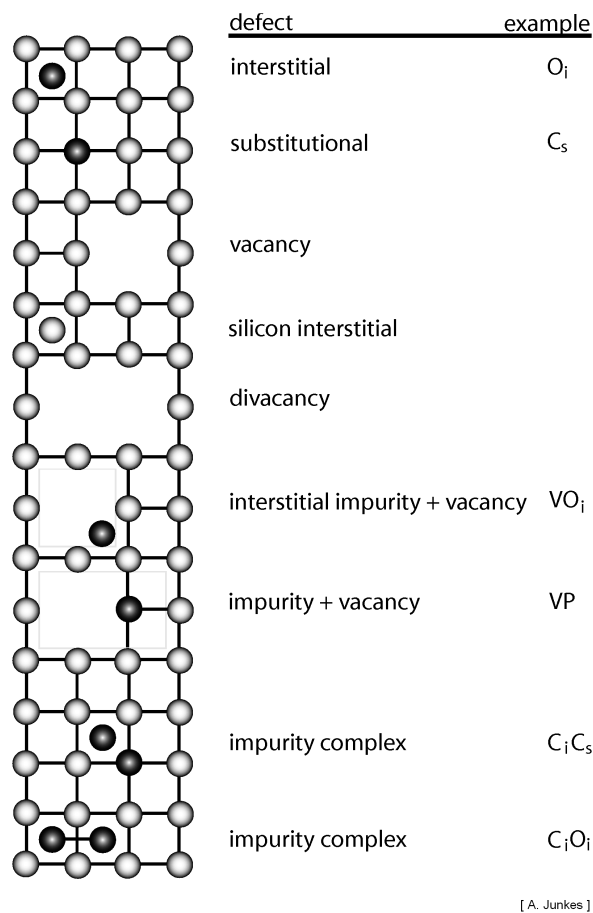

Figure 2.8: Point defects in a silicon lattice schematically. Vacancies, interstitial atoms (index i) and substitutional atoms (index s) are possible.

2.4.2 Defect Kinetics and Annealing

Due to the high mobility of vacancies and Si interstitials at temperatures above 150 K, approximately 60 % of the Frenkel pairs recombine, in cluster regions even 75 to 95 %. The remaining interstitials and vacancies react with each other or with impurities in the Si crystal and thereby can build electrically active defects. In Figure 2.8 some point defects are shown. Electrically active defects alter the macroscopic detector parameters, i.e. the depletion voltage, the doping type, the reverse current and the charge collection efficiency.

Defects can be acceptor- or donor-like and thereby change the effective doping concentration N_{eff}. Defects with an energy level in the band gap close to the band edges are called shallow defects. Defects close to the middle of the band gap are called deep defects.

The change of defects due to defect kinetics is called annealing. For neutron irradiated n-type silicon, previous investigations have shown that during short term annealing the effective doping concentration is reduced. This can be caused either by donor introduction or acceptor reduction. Microscopic measurements support the latter assumption.

2.4.3 Depletion Voltage and Type Inversion

Donor- and acceptor-like defects change the effective doping concentration N_{eff}. It is also possible that initial donors or acceptors are removed by certain defect reactions which again influences N_{eff}. Changes in N_{eff} will also influence the full depletion voltage U_{dep} which is proportional to $|N_{eff}|$ (see Equation 2.5).

If the sign of N_{eff} changes due to a high number of defects we have effectively a different doping type. This effect is called type inversion or space charge sign inversion.

2.4.4 Trapping and Charge Collection Efficiency

Radiation induced defects also can act as trapping centres: they can capture charge carriers (trapping) and re-emit them later (detrapping). If the detrapping time constant is large with respect to the integration time, the trapped particles do not contribute to the measured signal. This leads to a charge carrier loss and thus reduces the charge collection efficiency (CCE) of the diode.

Trapping can be described as a loss of free charge carriers N using the trapping time τ as

$$\mathrm{d}N = -\Sigma_i N \frac{1}{\tau_i} \mathrm{d}t = -N \frac{1}{\tau_{eff}} \mathrm{d}t. \tag{2.17}$$

The index i runs over all trapping defects and τ_{eff} is the effective trapping time of the diode. More precisely we have different values $\tau_{eff}^{e,h}$ for electrons and holes. The trapping probability for each trapping defect i can be written as

$$\frac{1}{\tau_i} = N_i \cdot \sigma_i \cdot v \tag{2.18}$$

with the concentration of unfilled trapping centres N_i and the trapping cross section σ_i. For the velocity of the charge carriers v usually the thermal velocity v_{th} is used, which is regarded to be fast compared to the drift velocity [Kra01]. However, it is not clear whether this approximation is still valid for very high electric fields and for drift velocities close to the saturation velocity.

In analogy detrapping of $N_{trapped}$ electrons (or holes) can be described with an effective detrapping time $\tau_{eff}^{detrapping}$ as

$$\mathrm{d}N_{trapped} = N_{trapped} \frac{1}{\tau_{eff}^{detrapping}} \mathrm{d}t \tag{2.19}$$

[Kra01] and [Bro00] investigated 300 μm thick FZ and Cz silicon diodes irradiated with equivalent fluences of up to $3 \cdot 10^{14}$ cm^{-2} and consider τ to be an overall constant of the diode and hence independent of the applied voltage and of the local electric fields. According to [Bea99] the trapping time cannot be described by a simple number but increases with voltage for fluences greater than 10^{14} cm^{-2}. [Lan08] investigated trapping in EPI diodes irradiated up to equivalent fluences of $4 \cdot 10^{15}$ cm^{-2} and found that charge collection cannot be described with an overall constant trapping time. He proposed τ to be voltage dependent or electric field dependent and showed that a good description of the data is possible assuming that τ depends linearly on voltage.

There are different possible reasons for a voltage or field dependent trapping time τ. If we assume the trapping cross section σ to be smaller for high charge carrier velocities, τ would be larger for high electric fields. Another reason might be very fast field enhanced detrapping: If detrapping in strong electric fields is fast enough, reemitted particles can contribute to the current signal leading to less effective trapping at higher electric fields.

Charge Collection Efficiency (CCE)

As discussed above trapping of electrons or holes can reduce the charge collection efficiency if the detrapping time constant is sufficiently large. Furthermore it is possible that highly irradiated diodes can not be fully depleted and thus the sensitive volume is reduced. If electron-hole pairs which are created in the undepleted volume recombine due to a lack of electric field, they do not contribute to the charge collection and CCE decreases.

It is also possible that CCE increases due to charge multiplication in high electric fields, which are present for very high doping concentrations N_{eff}.

2.4.5 Reverse Current

The reverse current or leakage current increases due to defects in the middle of the band gap, which act as generation centres. Electron-hole pairs are continuously thermally generated.

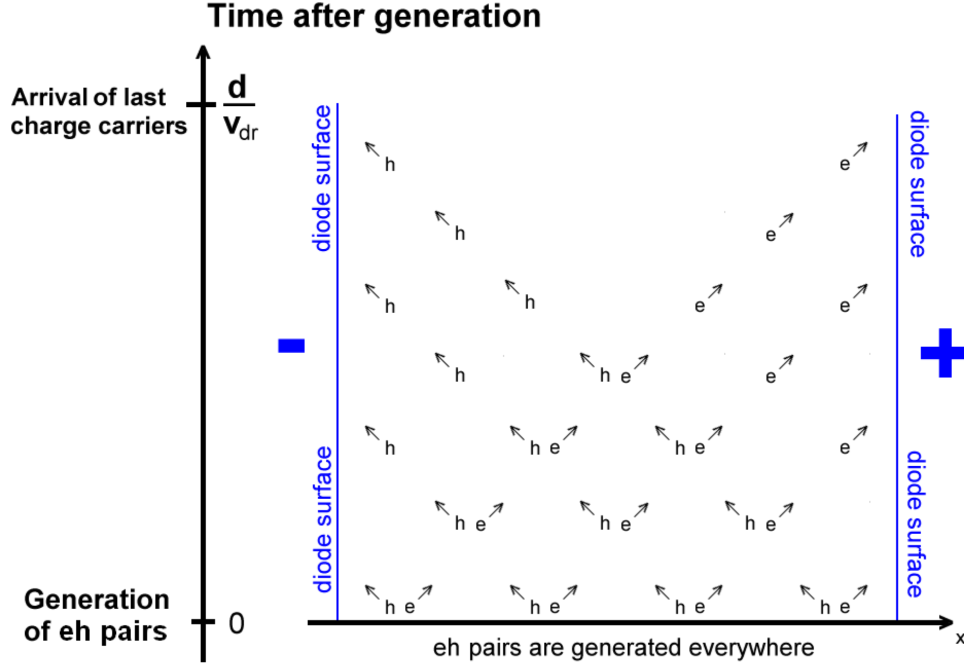

Figure 2.9: Reverse current in a silicon diode. The time development of electrons and holes is shown. For simplicity only those electron-hole pairs are shown which are generated at a fixed time $t = 0$. In this simple picture the drift velocity is assumed to be the same for electron and holes: v_{dr} = const.

2.4.6 Inhomogeneous Space Charge Distribution

In unirradiated diodes the reverse current is low and its effect on the space charge is negligible. For homogeneously doped silicon without irradiation defects the space charge distribution is thus homogeneous when fully depleted. For irradiated silicon the reverse current is increased and trapping centres are introduced. In the following the influence on the space charge distribution will be discussed.

The reverse current consists of both, electrons and holes. Let us assume to have the positive voltage applied on the right side of the silicon. Electrons will drift to the right side and holes to the left side. For a simple model of constant drift velocity this will lead to a linear distribution of free electrons and to a linear distribution of free holes inside the diode (see Figure 2.9). On the right side of the diode there will be a high number of free electrons. Electrons will constantly get trapped in trapping centres before they are released again (detrapping). If the number of trapping centres is large compared to the number of drifting electrons N, the time dependence of the number of trapped electrons $N_{trapped}$ depends on both, trapping and detrapping as follows:

$$\mathrm{d}N_{trapped} = \left(N \frac{1}{\tau_{eff}} - N_{trapped} \frac{1}{\tau_{eff}^{detrapping}} \right) \mathrm{d}t. \tag{2.20}$$

Equilibrium is given for $\mathrm{d}N_{trapped} = 0$. Solving the Equation for the number of trapped electrons $N_{trapped}$ gives

$$\mathrm{N}_{trapped} = N \frac{\tau_{eff}^{detrapping}}{\tau_{eff}} \tag{2.21}$$

Equation 2.21 shows that the number of trapped electrons is proportional to the number of free electrons. In analogy the number of trapped holes is proportional to the number of free holes. Hence the space charge distribution will be influenced by both, a linear distribution of free charge carriers (more electrons on the left side and more holes on the right side) and a linear distribution of trapped charge carriers.

Instead of a homogeneous space charge distribution we now have a linear space charge distribution and thus a quadratic electric field distribution.

Chapter 3

Experimental Setup

In this chapter first the investigated samples will be presented. Then the CV-IV measurements and the transient current technique (TCT) will be explained.

3.1 Investigated Samples and Irradiation

3.1.1 Material

In this work pad diodes of two different sizes, $(2.5\ \text{mm})^2$ and $(5\ \text{mm})^2$, and two different impurity concentrations, EPI-ST and EPI-DO, are investigated. The diodes are made from epitaxial n-type silicon grown by ITME[1]. They have active layers of two different thicknesses d (100 μm and 150 μm) and are grown on a highly doped Cz substrate of about 500 μm thickness (see Figure 3.1 b). The oxygen concentration is in the order of $10^{17}\ \text{cm}^{-3}$ ($2.8 \cdot 10^{17}\ \text{cm}^{-3}$ for the 100 μm thick EPI-DO, $1.4 \cdot 10^{17}\ \text{cm}^{-3}$ for the 150 μm thick EPI-DO and $0.45 \cdot 10^{17}\ \text{cm}^{-3}$ for the 150 μm thick EPI-ST diodes, average values. Also compare Figure 2.1). The doping concentration (phosphor) is in the order of $10^{13}\ \text{cm}^{-3}$ and will be determined in CV-IV measurements (see Table 5.1).

3.1.2 Structure

The diodes were processed by CiS[2]. A p^+ layer (highly doped p-type silicon) of about 1 μm thickness with a doping of approximately $10^{19}\ \text{cm}^{-3}$ at the front side provides the p-n junction. Aluminium structures were added to the front side including a pad with illumination window and a guard ring (see Figure 3.1 a). The pad is used to apply the voltage at the front side on a defined area. The pad area is $(2.5\ \text{mm})^2$ for the small diodes and $(5\ \text{mm})^2$ for the big diodes. The guard ring is needed to separate surface currents and to avoid break downs. The illumination window is used in TCT measurements to generate electron-hole pairs by laser light.

[1] Institute of Electronic Materials Technology (ITME), Warsaw, Poland.
[2] CiS Institut für Mikrosensorik GmbH, Erfurt, Germany.

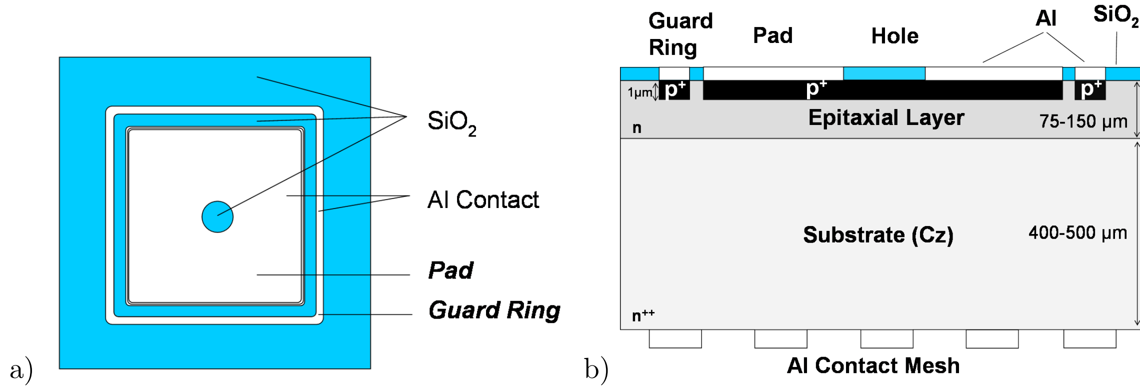

Figure 3.1: a) Schematic top view (front side) and b) cross section of the used pad diodes by [Koc07] and [Lan08].

Material	Device Label	d [μm]	Φ_n [10^{15} cm^{-2}]
EPI-DO	261636-11-45-3	150	0
EPI-DO	261636-11-25 (big)	150	0.1
EPI-DO	261636-11-27 (big)	150	0.3
EPI-DO	261636-11-14-1	150	1
EPI-DO	261636-11-39-1	150	2
EPI-DO	261636-11-20-1	150	3
EPI-DO	261636-11-45-1	150	4
EPI-ST	261636-14-45-3	150	0
EPI-ST	261636-14-14-1	150	1
EPI-ST	261636-14-39-1	150	2
EPI-ST	261636-14-56-1	150	3
EPI-ST	261636-14-29-1	150	4
EPI-DO	261636-4-14-2	100	0
EPI-DO	261636-4-14-1	100	1
EPI-DO	261636-4-39-1	100	2
EPI-DO	261636-4-56-1	100	3
EPI-DO	261636-4-12-1	100	4

Table 3.1: List of diodes investigated in this work. The fluence uncertainty is about 10 %.

3.1.3 Irradiation

Irradiation had been performed with neutrons from the research reactor of the Jozef Stefan Institute in Ljubljana. The 1 MeV neutron equivalent fluence values ϕ varied from $1 \cdot 10^{14}$ cm^{-2} to $4 \cdot 10^{15}$ cm^{-2}. A list of all investigated diodes and irradiation can be found in Table 3.1.

3.2 CV-IV Measurements

Both, the capacitance C between the pad and the back side of the diode and the bulk current I between pad and back side were measured in a probe station at different bias voltages U_{bias}.

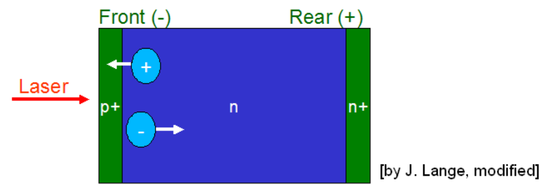

Figure 3.2: Movement of charge carriers after electron-hole pair production on the front side.

A Keithley Kei6517 (max. 1000 V, 1 mA) was used as bias source. In this work all CV-IV measurements were performed with a positive voltage applied to the back side. The guard ring and the pad at the front side were grounded. The measurements were performed at room temperature and in the dark to avoid photo currents.

3.2.1 CV Measurements

The capacitance between pad and back side was determined in parallel mode using a Hewlett Packard HP4263 capacitance bridge. For the CV measurements of irradiated diodes the measured capacitance depends on frequency and temperature. When the depletion voltage was extracted from CV measurements it turned out to agree best with the depletion voltage extracted from charge collection efficiency measurements if a frequency of 10 kHz at room temperature was used. In this work CV measurements are performed at room temperature with an AC voltage with a frequency of 10 kHz and an amplitude of 0.5 Volt added to the DC bias voltage if not denoted otherwise.

3.2.2 IV Measurements

The current between pad and back side is measured using the current meter of the Kei6517 used as a bias source. The measured current is the bulk current generated in the diode volume under the pad. The surface current and the bulk current of the diode volume close to the surface is collected at the guard ring.

3.3 Transient Current Technique (TCT)

For the transient current technique (TCT) electron-hole pairs are created inside of the diode. In this work red laser light with an absorption length of about 3 μm was used to create the electron-hole pairs at the front side of the diode. For the measurements a reverse bias voltage is applied. The electrons drift to the back side of the diode inducing a current which is read out by an oscilloscope. The holes are collected almost immediately at the front side as indicated in Figure 3.2 and hence have negligible contribution to the total current signal measured.

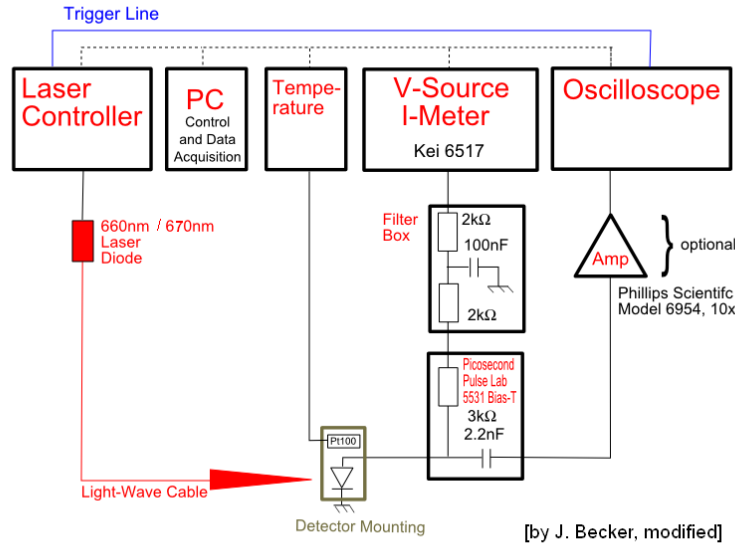

Figure 3.3: The used laser TCT setups schematic.

3.3.1 The Different TCT Setups

In the detector laboratory different TCT setups are available. The TCT setups relevant for this work are the Multi Channel TCT (MTCT), the TCT setup 3 (TCT3) and the TCT setup 4 (TCT4). An overview valid for all of these TCT setups is shown in Figure 3.3.

At all setups a negative voltage is applied to the pad on the front side of the diode (front biasing), the guard ring is floating and the back side is grounded. The TCT current signal is decoupled from the DC reverse current using a bias-T before it is read out with a digital oscilloscope. The voltage source is controlled and all data is stored using the computer. An amplification of the decoupled current signal is possible and the temperature can be controlled using a PT100 temperature sensor. The oscilloscope is triggered externally by the laser controller.

Multi Channel TCT (MTCT)

A red laser with 660 nm wavelength manufactured by Picoquant GmbH with a pulse width of 70 ps (FWHM) is used. The laser light is led into an optical system. The position of the focus can be controlled mechanically in x, y and z direction with a precision of 0.1 µm. Different spot sizes on the diode surface are possible. They can be measured by scanning the edge of the illumination hole using the position control. For all MTCT measurements performed in this work the laser light spot was centred on the illumination hole of the diode, while the spot size was varied in order to obtain different charge carrier densities.

At the MTCT setup the diode is laid into a metal holder and the front side is biased using a needle. Measured signal heights varied by sometimes up to 20 percent when mounting and demounting the same diode. This instability is possibly caused by difficulties with the back side contact between the diode and the metal holder. However, Using a vacuum pump on the

diode back side did not solve the problem. Due to this instability CCE measurements made on this setup were not used to fit the trapping time.

The oscilloscope used is the Tektronix DPO 7254 with 2.5 GHz bandwidth and the rise time achieved for the small 150 µm diodes is 600 ps. Data taken at this setup was used for the analysis with the charge correction method (see Section 4.2).

TCT Setup 3 (TCT3)

For the TCT setup 3 a red laser with 670 nm wavelength manufactured by Advanced Laser Diode Systems is used. The pulse width is 30 ps (FWHM). Alternatively an infrared laser (1060 nm) with a pulse width of 50 ps (FWHM) can be used. The TCT3 can be cooled down to -20 °C.

At the TCT3 the diode is fixed with a vacuum pump on a copper chuck and the front side is biased using a needle. The signal height is stable within ±1%. The oscilloscope used is the Tektronix DPO 4104 with 1 GHz bandwidth. Due to rise times of greater than 1 ns no time structure in the TCT current signal could be measured for any of the examined diodes. It was used for CCE measurements before it was replaced by the TCT setup 4.

TCT Setup 4 (TCT4)

For the TCT setup 4 the same lasers (670 nm and 1060 nm) and the same oscilloscope as for TCT3 are used. The diode mounting is improved and additionally to the liquid cooling system used at TCT3 there is a Peltier element implemented. Temperatures down to -40 °C are possible.

The diode is fixed with a vacuum pump on a gold-plated metal chuck and the front side is biased using a needle. Since February 2010 stable CCE measurements are possible with a time resolution of 650 ps rise time for the small 150 µm thick diodes. All time resolved measurements which were evaluated with the charge collection simulation were performed at this setup.

In order to achieve this time resolution the connection between the chuck and the signal cable needed to be improved. A short and relatively massive connection turned out to work best in terms of time resolution.

3.3.2 Laser Output Power Stability

As signal stability is required for a reliable CCE determination the laser output power was investigated at both setups, MTCT and TCT4. After switching the laser on, its output power increases until the final output power is reached. Figure 3.4 shows the signal stability of the 670 nm laser used at TCT4. The signal refers to the collected charge, i.e. the integrated TCT current. At night time the signal varies by up to 0.3 percent around its average value. At day time the fluctuations are larger. A possible reason might be a higher temperature variation at day time due to annealing studies in the same room. Laser stability for the MTCT setup was

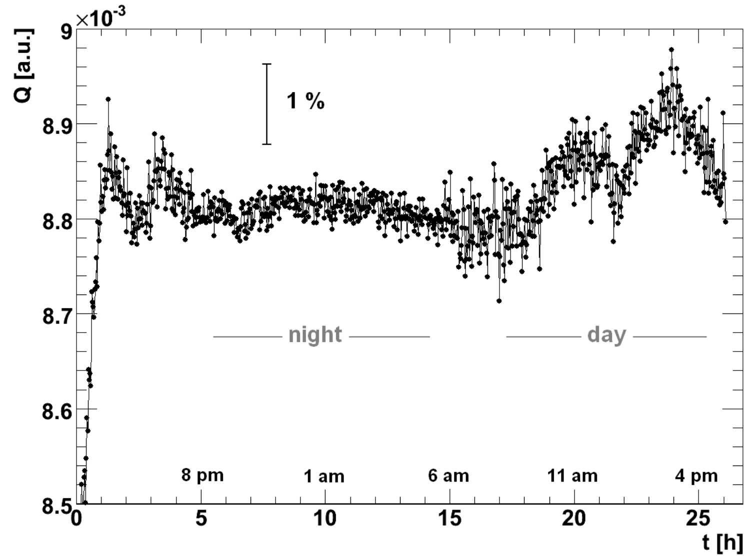

Figure 3.4: The collected charge Q (integrated current signal) versus time. An unirradiated diode and the red laser at the TCT setup 4 were used. The laser was switched on at $t = 0$.

operation time	relative power in percent
15 min	80
30 min	89
60 min	96
90 min	100
all later measurements	100 ± 0.3

Table 3.2: Laser stability at the MTCT setup. The relative laser output power is measured with an unirradiated diode by integration of the current signal (normalised). Time windows of up to 9 hours were used.

investigated during the day only and showed a similar behaviour as the TCT4 setup at night time. The signal development for the MTCT setup is summarised in Table 3.2.

3.3.3 Determination of the Collected Charge Q

We tried two different ways to measure the collected charge Q. Offline integration of the measured TCT current signal and analogue integration using a charge sensitive amplifier.

Offline Integration

The TCT current signal I as measured at the oscilloscope is recorded. Later the amount of collected charge Q is determined by taking the integral of I (see Figure 3.5). The same integration time window is used for all measurements to be compared.

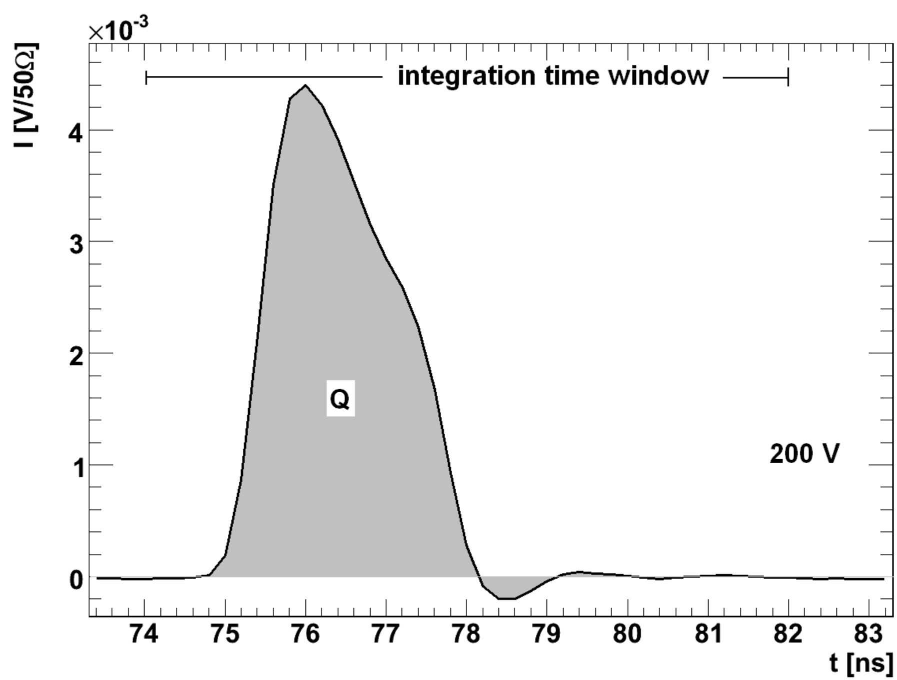

Figure 3.5: Determination of the collected charge Q by offline integration of the TCT current signal for an unirradiated diode at 200 V.

Analogue Integration

As an alternative way to determine the collected charge we used analogue integration of the TCT current signal by replacing the current amplifier of the TCT setup (see Figure 3.3) with a charge sensitive amplifier and a shaping amplifier. Different shaping times are selectable. The charge sensitive amplifier is built in such a way that the amplitude of the output current is proportional to the collected charge.

3.3.4 Determination of the Charge Collection Efficiency

The charge collection efficiency (CCE) is defined as the ratio of collected charge Q to deposited charge Q_0:

$$CCE = \frac{Q}{Q_0} \tag{3.1}$$

In order to determine the CCE experimentally, both, the charge measured by the oscilloscope, Q, and the initially deposited charge, Q_0, must be known. For unirradiated diodes trapping is negligible and $Q = Q_0$. Thus when integrating the TCT signal of an unirradiated diode we obtain the deposited charge Q_0. In order to reduce the uncertainty of Q_0, unirradiated diodes are measured before and after each irradiated diode is measured.

When the collected charge was determined by offline integration the measured CCE curves were the same for different TCT setups. Using the charge sensitive amplifier the CCE curves depend on the shaping time used. In Figure 3.6 CCE curves measured with different shaping times at TCT3 are compared with each other and with offline integration at TCT3 and TCT4. Higher CCE for higher shaping time is seen. This effect could hint at detrapping: detrapped electrons contribute to the collected charge only when detrapping takes place during the integration time window. Increasing the shaping time and hence the integration time will lead to more detrapping seen in the signal.

We see that the noise for offline integration is sufficiently low compared to analogue integration (compare Figure 3.6) and we choose to determine the collected charge Q by offline integration for the following analysis.

3.3.5 Charge Carrier Density Effects

In order so simulate the charge collection, the knowledge of the electric field distribution is needed. Charge carrier densities in the order of the doping concentration change the local electric field significantly and the charge collection time increases.

Charge carrier density effects were studied at the MTCT setup by changing the laser spot size and using optical attenuators. With the laser light focussed on the diode surface, changes in the charge collection behaviour were found.

When focussed to an area of approximately $(40\mu m)^2$ the charge carrier density is in the order of 10^{15} cm^{-3}. When focussed to an area of approximately $(800\mu m)^2$ the charge carrier

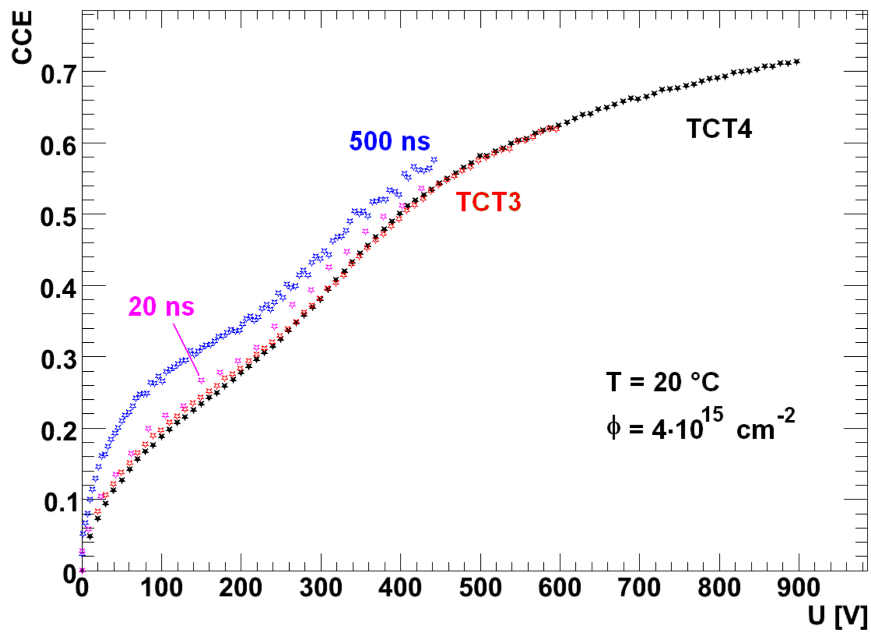

Figure 3.6: Comparison of CCE curves for different shaping times at the TCT3 with the charge sensitive amplifier and offline integration for TCT3 and TCT4.

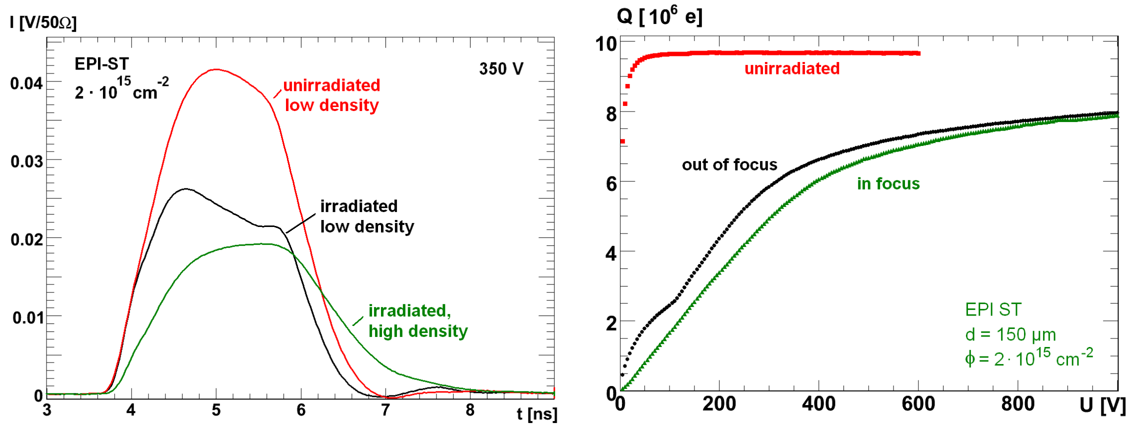

Figure 3.7: Charge carrier density effects on the charge collection for an irradiated EPI-ST diode with a neutron fluence of $2 \cdot 10^{15}$ cm^{-2}. TCT current signal (left) and collected charge (right) compared to an unirradiated diode. The charge collection time and hence trapping effects increase when the charge carrier density is in the order of the doping concentration.

density is in the order of $2.5 \cdot 10^{12}$ cm^{-3}. Figure 3.7 shows the TCT current signal and the CCE for both cases.

For the high charge carrier density changes of the electric field appear: Inside of the electron-hole cloud the electric field is screened and reduced. Consequently the drift velocity is reduced and the collection time increases. Due to the increased charge collection time it becomes more likely that charge carriers get trapped and the CCE decreases.

For the later analysis we could avoid charge carrier density effects by using unfocussed lasers and optical attenuators.

Chapter 4

Analysis

In this chapter the analysis of both, CV-IV measurements and TCT measurements will be presented.

CV-IV measurements are used to extract the full depletion voltage U_{dep} and to find out whether type inversion took place due to irradiation. The effective doping concentration N_{eff} and hence the space charge is determined from U_{dep} assuming a homogeneous space charge distribution. Diode thickness will be determined and neutron fluences will be reviewed.

TCT measurements are analysed using two different methods to extract the effective trapping time τ_{eff}, the charge correction method (CCM) and a simulation of charge collection. Furthermore the space charge distribution is extracted from the TCT current signal using the simulation.

4.1 CV Measurements

4.1.1 Determination of the Diode Thickness

For unirradiated diodes we know that the capacitance changes with bias voltage if not fully depleted and saturates if fully depleted. The diode thickness is determined from the CV measurements before irradiation according to Equation 2.7. The thickness is then given by

$$d = \epsilon\epsilon_0 \frac{A}{C_{end}}, \tag{4.1}$$

with the saturation capacitance for a fully depleted diode C_{end} (see Figure 4.1).

4.1.2 Determination of the Depletion Voltage

For both, unirradiated and irradiated diodes the full depletion voltage U_{dep} is determined in the following way: We present the measured CV curve in a double logarithmic scale. A linear fit in the region of highest slope is made and its intersection with the saturation capacitance C_{end} is determined as seen in Figure 4.1. The point of intersection defines the depletion voltage U_{dep}.

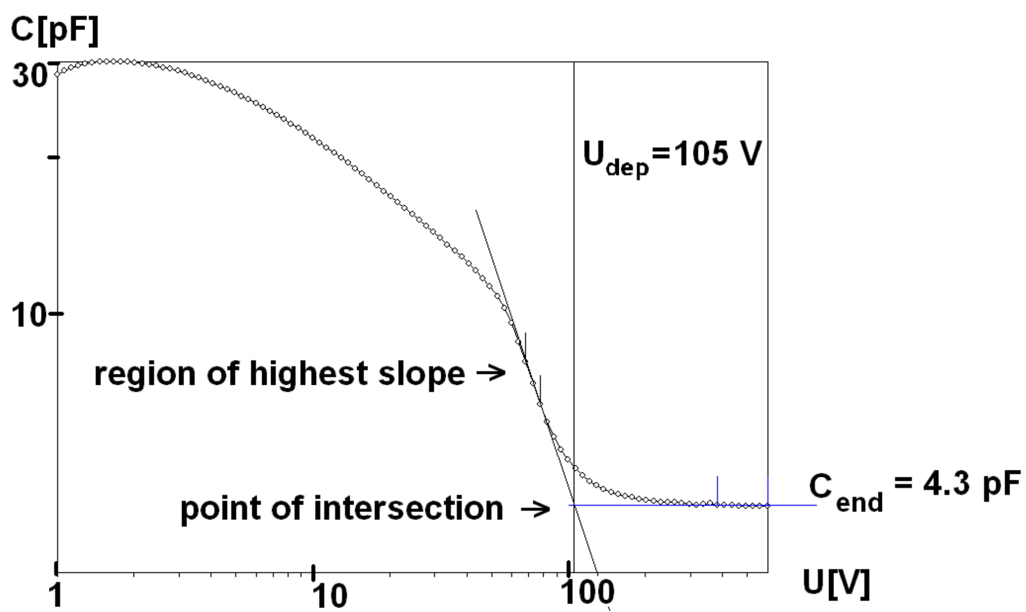

Figure 4.1: Determination of the depletion voltage U_{dep} and of the saturation capacitance C_{end} for an irradiated 150 µm thick EPI-DO diode with a neutron fluence of 10^{15} cm^{-2} at 20 °C and 10 kHz.

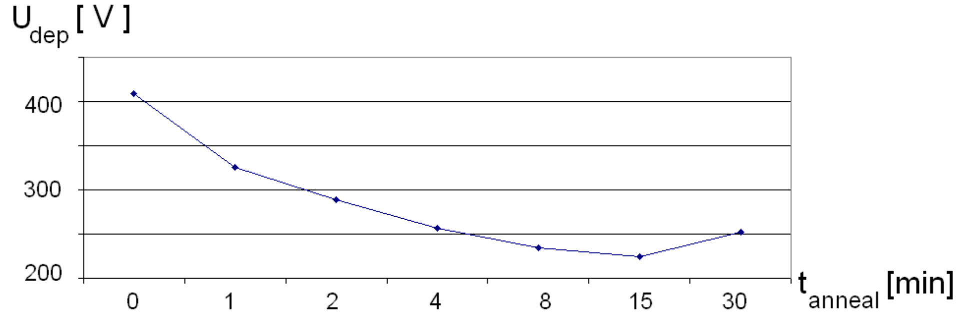

Figure 4.2: U_{dep} annealing behaviour at 80 °C for a 150 µm EPI-DO diode, after neutron irradiation with a fluence of $2 \cdot 10^{15}$ cm^{-2}.

4.1.3 Determination and Description of the Space Charge

For unirradiated diodes with homogeneous doping we have a homogeneous space charge distribution if fully depleted. In this case the depletion voltage U_{dep} is proportional to the absolute value of the space charge density $|N_{eff}|$. For n-type silicon we have positive space charge and we can calculate the space charge density according to Equation 2.5:

$$N_{eff} = \pm \frac{2\epsilon\epsilon_0}{d^2 q_0} U_{dep}. \tag{4.2}$$

The same procedure can be performed for irradiated diode under the approximation of a homogeneous space charge distribution. In this case we need to extract the sign of N_{eff} from annealing studies explained below.

Annealing Behaviour and Type Inversion

For neutron irradiated silicon diodes the effective number of acceptors decreases during short term annealing (see Section 2.4.2). For materials with negative space charge this leads to a decrease of the absolute value of the effective doping concentration $|N_{eff}|$ and hence to a decrease of the depletion voltage U_{dep} during short term annealing as seen in Figure 4.2. For materials with positive space charge, e.g., n-type materials before type inversion, an increase of both $|N_{eff}|$ and U_{dep} is expected.

If an n-type diode shows a decrease in depletion voltage during short term annealing after neutron irradiation we conclude that we have negative space charge and that type inversion took place.

Irradiation-Induced Change of Space Charge with Fluence

In order to describe the change in U_{dep} and N_{eff}, we study the change of effective space charge due to irradiation and parameterise according to the Hamburg Model as follows:

$$N_{eff,0} - N_{eff}(\phi) = N_r \left(1 - e^{-c\phi}\right) + g\phi. \tag{4.3}$$

$N_{eff,0}$ denotes the space charge density before irradiation and $N_{eff}(\phi)$ the space charge density after irradiation with neutron fluences ϕ. All values refer to 8 minutes annealing at 80 °C. The first term describes the donor removal and the second term the introduction of space charge. $N_r \leq N_{eff,0}$ is the density of the initial doping which will be removed by irradiation and c is called removal constant and describes the removal velocity. g is the effective space charge introduction rate and can also be written as the difference between donor and acceptor introduction rate $g = g_A - g_D$. See [Lan08] or [Kra01] for more details.

4.2 Charge Correction Method

The charge correction method (CCM) according to [Kra01] is a method to determine the effective trapping time in irradiated diodes. A TCT current signal with sufficient time resolution for different voltages above depletion is needed.

4.2.1 Assumptions

Constant Trapping

The effective trapping time is assumed to be an overall constant τ_{eff} in each diode for a given irradiation. Hence it is assumed to be independent of the local electric field and of the applied voltage.

Fast Injection

The injection time of free charge carriers is assumed to be small compared to the charge collection time. In our case we use laser light with a time width of 70 ps FWHM and collection time is in the order of 2 ns for the here investigated 150 µm thick diodes.

Sufficient Time Resolution

Electronic distortions due to the setup and the corresponding electronic circuit are neglected. This assumption is problematic, since the time resolution of the used MTCT setup is characterised by 600 ps rise time for the small 150 µm thick diodes. It is not clear whether the charge collection time of 2 ns is sufficiently large to avoid systematic errors.

Full Depletion

The CCM is usually used for fully depleted diodes only. In not fully depleted diodes very low electric fields occur and cause the charge collection time to be very long. In this case it is difficult to define an appropriate integration time window and detrapping of charge carriers might becomes relevant.

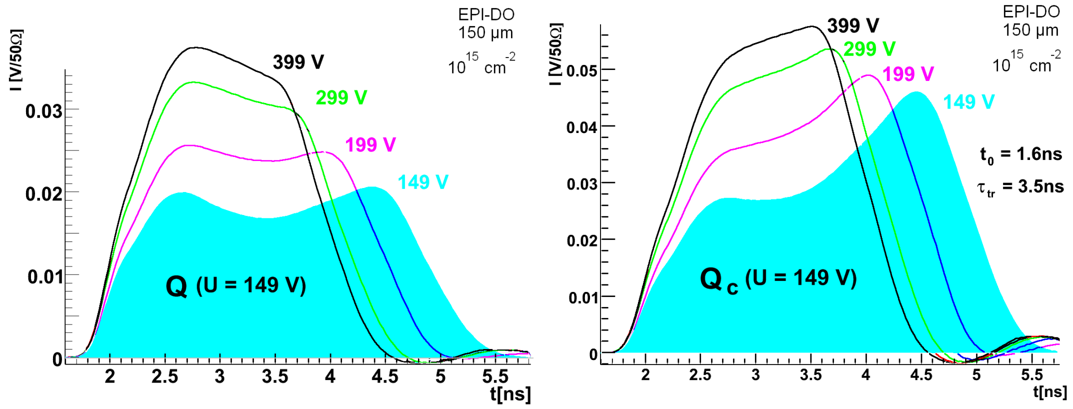

Figure 4.3: Raw (left) and trapping corrected (right) TCT current signal for the 150 µm EPI-DO diode with $\phi = 10^{15}$ cm^{-2}.

One Charge Carrier Type Only

Due to the short laser absorption length of 3 µm we can neglect the hole drift. Only electrons contribute to the current signal.

Number of Drifting Electrons

Since the trapping time is assumed to be constant ($\tau = \tau_{eff} = $ const) and detrapping is neglected, the number of drifting electrons will decrease exponentially with time (compare Equation 2.17) and is given by

$$N(t) = N_0 \cdot \exp\left(\frac{t_0 - t}{\tau_{eff}}\right), \qquad t \in [t_0, t_0 + t_c] \tag{4.4}$$

where τ_{eff} denotes the effective trapping time constant, t_0 is the time of electron injection, $N_0 = N(t_0)$ the number of injected electrons and t_c the collection time.

4.2.2 Compensation of Trapping

According to [Kra01] the measured TCT current signal $I(t)$ now can be corrected to compensate trapping effects in the following way:

$$I_c(t) = I(t) \exp\left(\frac{t - t_0}{\tau_{tr}}\right). \tag{4.5}$$

τ_{tr} is the trapping correction time. If τ_{eff} is the trapping time of the irradiated diode trapping is completely compensated if the signal is corrected with τ_{tr}=τ_{eff}. Figure 4.3 shows the TCT current signal before and after correction for an irradiated diode.

The collected charge Q can be calculated by integrating the measured TCT current signal

I:

$$Q = \int I(t)\mathrm{d}t \tag{4.6}$$

If we replace the measured current I by the corrected current I_c we obtain the trapping corrected charge Q_c:

$$Q_c = \int I_c(t)\mathrm{d}t \tag{4.7}$$

The integration time window will be discussed in the following.

4.2.3 Data Preparation

Electronic distortions cause the current we measure not to be equal to the current in the diode. While effects of the diode capacitance can be calculated and deconvoluted other distortions remain. Reflections at connectors and oscillations due to inductances occur.

Deconvolution

Due to the diode capacitance the TCT current signal measured at the oscilloscope I is smeared in time (rise time 600 ps). However, for the CCM the original current signal in the diode is required. According to [Kra01] the signal can be deconvoluted if we assume that the electronic circuit is described by an ideal diode capacitance C and the input impedance of the oscilloscope R. The deconvoluted current signal than is

$$I_{deconv}(t) = \tau_{RC}\frac{\mathrm{d}I(t)}{\mathrm{d}t} + I(t), \tag{4.8}$$

with $\tau_{RC} = RC$. Figure 4.4 shows the deconvoluted signal for $R = 50\ \Omega$ and different values of C. An undershoot at the end of the deconvoluted current signal appears. This might be due to inductances in the setup which were not deconvoluted. Both TCT current signals, the raw signal and the deconvoluted signal, were used and results were compared.

Reflections and Oscillations

Reflections and oscillations seen at the oscilloscope are not directly produced by drifting charge carriers inside of the diode. The exponential correction of the measured current (see Equation 4.5) enhances the reflections and oscillations. This can cause systematic errors to the corrected charge and thus can affect the results of this method.

It is necessary to define appropriate integration time windows in order to limit the effects of electronic distortions after the signal. Different time windows are used to find out how much the results are dependent on this criterion. Two methods are used: either the same integration time window for all voltages is used or the signal is cut off after the signal returned to some defined value close to zero.

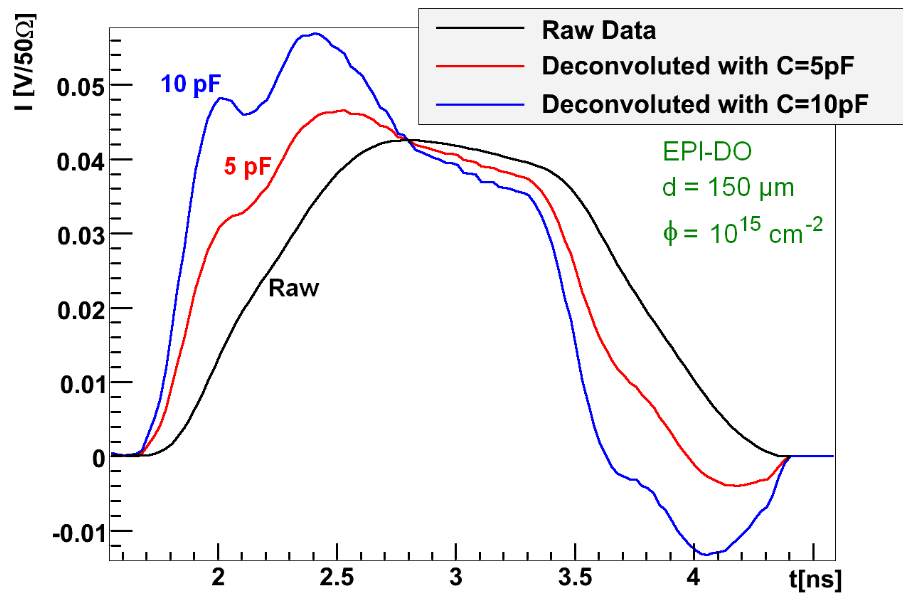

Figure 4.4: Deconvolution of the TCT current signal with different capacitances C.

Determination of the Trapping Time by the Zero-Slope Condition

In Section 2.3 we have seen that for irradiated diodes with trapping (trapping time τ_{eff}) but without charge multiplication effects, the CCE value is always below 1, i.e. the measured charge $Q(U)$ is smaller than the deposited charge Q_0. For higher voltages the charge collection time decreases and less electrons are trapped resulting in more collected charge. Hence without trapping correction $Q(U)$ has a positive slope:

$$\text{no correction} \Rightarrow Q(U) < Q_0, \frac{dQ}{dU} > 0 \tag{4.9}$$

If τ_{tr} is greater than τ_{eff} (τ_{eff} is the real trapping time of the examined diode) the trapping effects are not completely compensated and Q_c is still smaller than Q_0 and has a positive slope:

$$\tau_{tr} > \tau_{eff} \Rightarrow Q_c(U) < Q_0, \frac{dQ_c}{dU} > 0 \tag{4.10}$$

If $\tau_{tr} = \tau_{eff}$, the corrected current $I_c(t)$ will correspond to the theoretical TCT signal as if no trapping would take place. The corrected charge Q_c is than equal to the deposited charge Q_0. Since Q_0 is constant for different voltages, Q_c will also be voltage independent:

$$\tau_{tr} = \tau_{eff} \Rightarrow Q_c(U) = Q_0 = \text{const}, \frac{dQ_c}{dU} = 0 \tag{4.11}$$

For τ_{tr} smaller than τ_{eff} the trapping effects are overcompensated. This leads to a corrected charge Q_c being greater than the originally deposited charge with negative slope:

$$\tau_{tr} < \tau_{eff} \Rightarrow Q_c(U) > Q_0, \frac{dQ_c}{dU} < 0 \tag{4.12}$$

If τ_{eff} is not known it can be determined by the condition of a voltage independent $Q_c(U)$ curve above depletion. Different values of τ_{tr} are used and for $U > U_{dep}$ a linear fit of $Q_c(U)$ is calculated. Figure 4.5 shows the voltage dependency of Q_c for different values of τ_{tr}.

The slope of the linear fit of the Q_c-curve is drawn as a function of the trapping correction time τ_{tr} (see Figure 4.6). The trapping correction time τ_{tr} which leads to a flat $Q_c(U)$ curve, i.e. which produces a linear fit with zero slope, is considered to be equal to the trapping time of the diode τ_{eff}.

As seen in Figure 4.5 Q_c is not constant for $U > U_{dep}$ even if the zero-slope condition is fulfilled. Hence it is not clear whether the compensation of trapping works as assumed. Different voltage ranges for the linear fit are tested in order to check the reliability of the method. If the CCM assumptions are correct the results should be independent on the voltage range chosen.

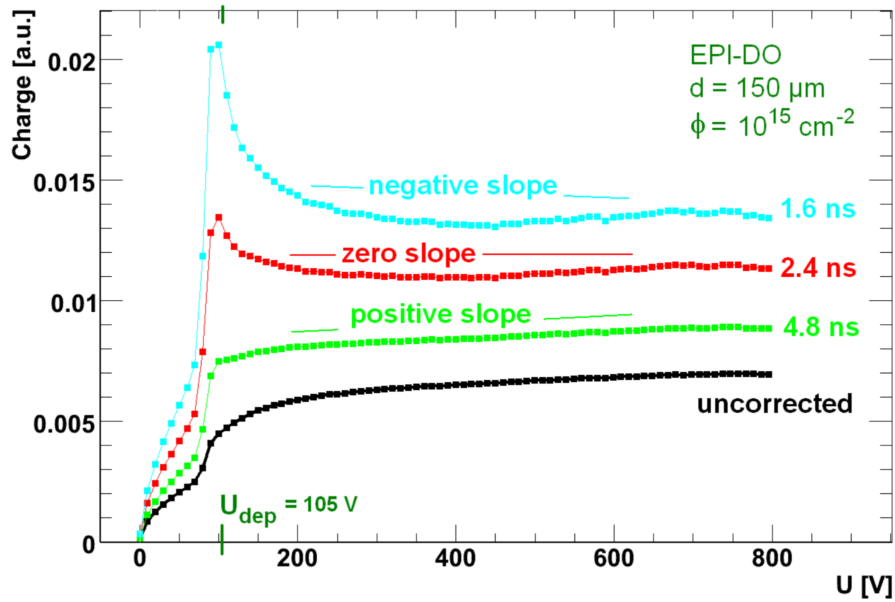

Figure 4.5: Corrected charge Q_c versus voltage for different values of the trapping correction time τ_{tr}. The slope is calculated by a linear fit above 120 V up to 800 V.

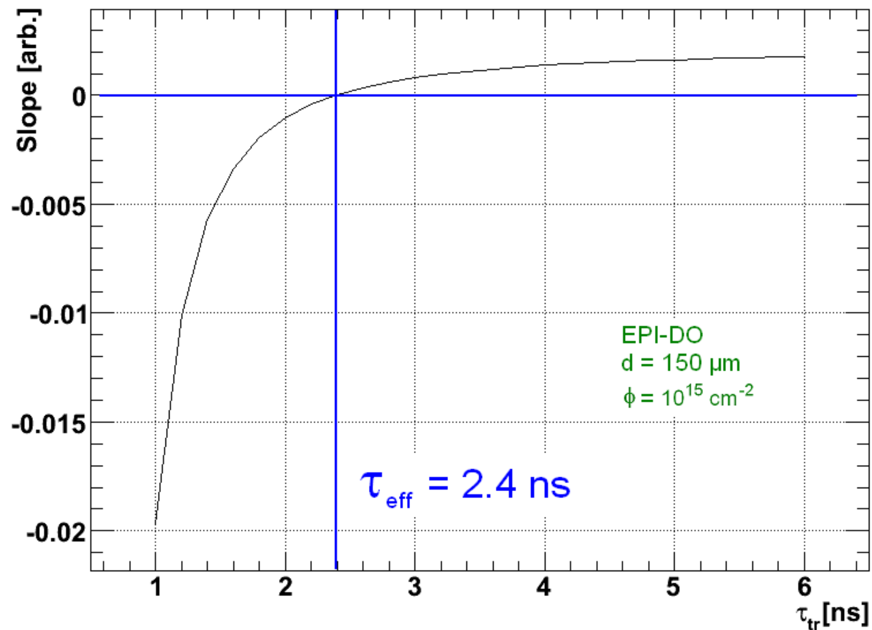

Figure 4.6: Slope of the linear fit of the $Q_c(U)$-curve above 120 V as a function of τ_{tr}. τ_{eff} is determined by the point with zero slope.

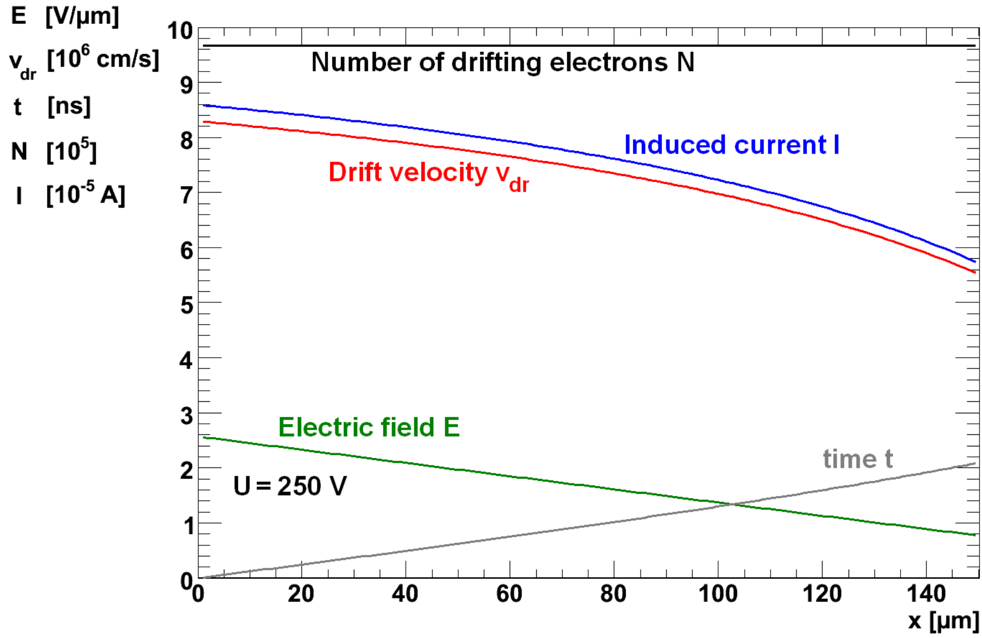

Figure 4.7: Calculated electric field, drift velocity and induced current for an unirradiated diode. The same y-axis is used for all quantities in given units. Electrons are created at position $x = 0$ at time $t = 0$. Due to the electric field E the electrons drift in x-direction inducing a current I until they reach $x = d$ at $t \approx 2$ ns.

4.3 Simulation of Charge Collection for Unirradiated Diodes

As discussed in Section 2.3 the induced current of N drifting electrons, all at the same position $x(t)$ in a planar diode, is given by

$$I(t) = \frac{q_0 N(t)}{d} v_{dr}(t). \tag{4.13}$$

The thickness d was determined by CV measurements before irradiation, q_0 is the elementary charge, $N(t)$ the number of drifting electrons and $v_{dr}(t)$ is the drift velocity. The induced current and the related quantities are shown in Figure 4.7. As seen in Equation 2.10 we have $t = t(x)$ and can either use time coordinates $I = I(t)$ or space coordinates $I = I(t(x)) = I(x)$.

4.3.1 Assumptions

Pure Electron Signal Starting at the Front Side

We neglect the contribution of the created holes to the TCT signal and assume that the electrons start drifting at the front side of the diode at position $x = 0$. The absorption length of the used laser light is 3 μm and thus small compared to the diode thickness d. Created holes will be almost immediately collected at the front side of the diode.

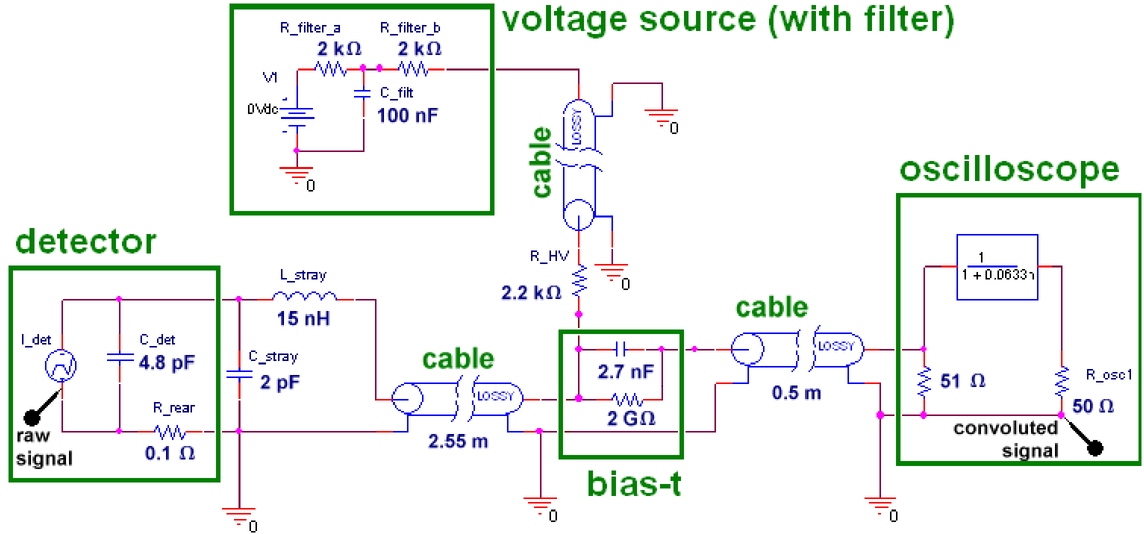

Figure 4.8: The electronic circuit of the TCT setup 4 as used for the SPICE simulation.

Very Short Laser Pulse

For the simulation we assume the laser pulse to be a delta function, i.e. all electrons start drifting at the time $t = t_0$. The time widths of the used laser light (FWHM < 80 ps) is small compared to the time resolution (rise time 600 ps) and to the charge collection time (2 ns).

Drift Velocity as Function of Electric Field

For the movement of the free electrons we use the drift model explained in Section 2.3.1 and the parameters for the electron drift in <100> direction by [Bec10]. We do not take into account diffusion.

No Trapping and Homogeneous Space Charge Distribution

For unirradiated diodes no trapping and a homogeneous space charge distribution is assumed, leading to a constant number of drifting electrons and to linear electric fields, respectively. The space charge and hence the electric field is extracted from the depletion voltage which was determined by CV measurements.

4.3.2 Circuit Simulation

Due to the experimental setup the current measured at the oscilloscope is not equal to the induced current in the diode. Electronic circuit effects smear the current signal. To take into account these effects the electronic circuit is simulated using SPICE[1]. Figure 4.8 shows the electronic circuit for the TCT setups.

[1]SPICE is a general-purpose analogue electronic circuit simulator. We used PSPICE by Cadence Design Systems, www.cadence.com.

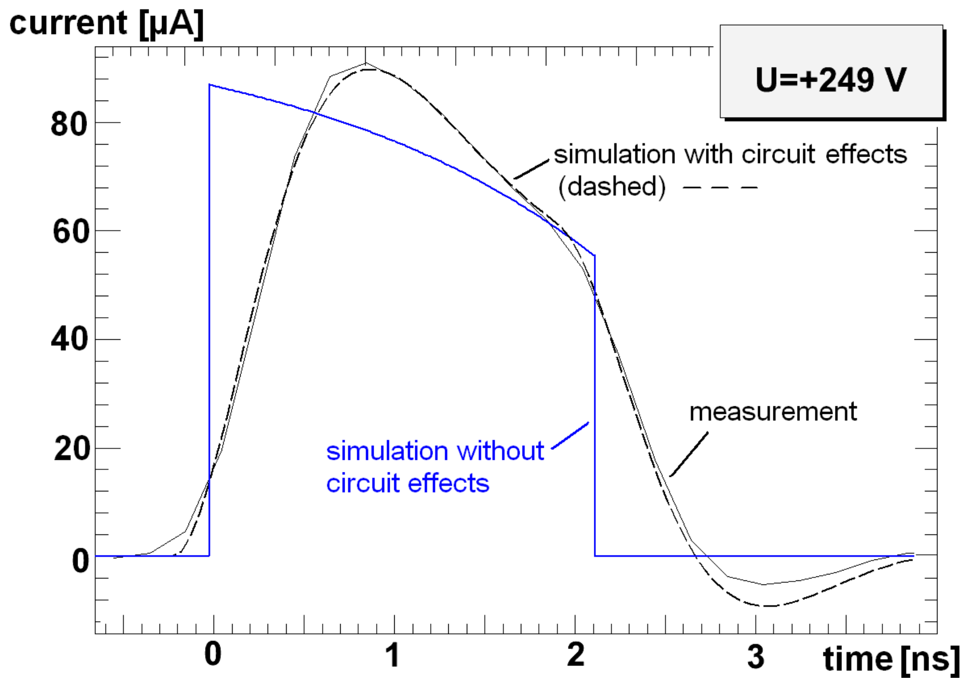

Figure 4.9: The simulated TCT current signal with and without circuit effects compared to measurement. $t = 0$ is chosen arbitrarily.

Comparison to Experimental Results

To fine tune the circuit simulation in SPICE comparisons to experimental results are performed. Stray capacitances and small inductances can be determined by comparing the measured signals with the simulated signals.

Figure 4.9 shows the simulated current signal $I(t)$ with and without electronic circuit effects compared to measurement. The signal without circuit effects is the same as seen in Figure 4.7. Good agreement between simulation with circuit effects and measurement is achieved.

4.3.3 Deposited Charge Q_0

Since no trapping occurs for unirradiated diodes the deposited charge is equal to the collected charge. In the simulation the number of deposited electrons N_0 is a free parameter. We choose N_0 in such a way that the collected charge is the same for simulation and experiment. Assuming no charge loss in the electronic circuit N_0 also is the number of deposited electrons in the experiment and the deposited charge is given by $Q_0 = q_0 \cdot N_0$.

4.4 Simulation of Charge Collection for Irradiated Diodes

In irradiated diodes the space charge distribution $N_{eff}(x)$ and the field dependent trapping time $\tau(E)$ are to be determined.

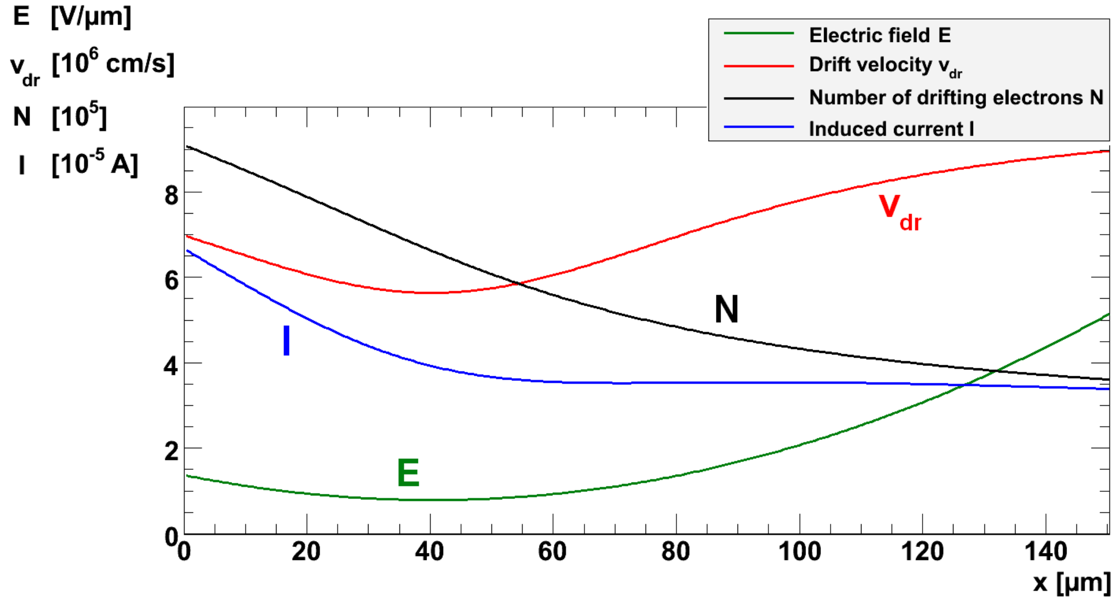

Figure 4.10: Calculated electric field, drift velocity and induced current for an irradiated diode. The same y-axis is used for all quantities in given units. $N_0 = N(x = 0)$ electrons are created at $x = 0$. During the drift some electrons are trapped until $N(x = d)$ electrons reach $x = d$. The trapping time is extracted from the CCE curve and the electric field is extracted from the TCT current signal.

For irradiated diodes some assumptions made for unirradiated diodes need to be modified. The thickness d was determined before irradiation. The effects on the electric field, on the number of drifting electrons, on the drift velocity and on the induced current are shown in Figure 4.10.

4.4.1 Assumptions

Trapping, Detrapping and Charge Multiplication

For irradiated diodes trapping is not negligible. We will describe trapping with a trapping time τ and allow it to depend on the electric field: $\tau = \tau(E)$. The change of the number of drifting electrons N is given by

$$\mathrm{d}N = -\frac{1}{\tau(E)} N \mathrm{d}t. \tag{4.14}$$

We do not simulate any other effects on the number of drifting electrons like detrapping or charge multiplication. If trapping centres with very short detrapping time[2] occur they will not contribute to the trapping time τ.

[2]Shallow trapping centres at room temperature have a very short detrapping time. The electron will be trapped only a short time.

Space Charge Distribution

In irradiated diodes trapping of an increased number of thermally generated charge carriers may cause an inhomogeneous space charge distribution $N_{eff}(x)$. As a first order approximation we will consider $N_{eff}(x)$ to be linear as motivated in Section 2.4.6. Hence we expect parabolic electric fields.

4.4.2 Deposited Charge Q_0

Each irradiated diode is compared to an unirradiated diode as described in Section 3.3.4. The same value of deposited charge Q_0 is used for both, unirradiated and irradiated diode.

4.4.3 Determination of Trapping Time by a CCE Fit

A comparison of the charge collection efficiency (CCE) for simulation and measurements is performed and different parameterisations for the trapping time $\tau(E)$ are compared.

Field independent trapping time

$$\tau = \tau_0 \tag{4.15}$$

Linearly field dependent trapping time

$$\tau(E) = \tau_0 + \tau_1 \cdot E \tag{4.16}$$

Linearly field dependent trapping probability

$$\frac{1}{\tau(E)} = \frac{1}{\tau_0} - \frac{1}{\tau_1} \cdot E \tag{4.17}$$

Trapping probability linearly dependent on the drift velocity

$$\frac{1}{\tau(E)} = \frac{1}{\tau_0} - \frac{1}{\tau_1} \cdot v_{dr}(E) \tag{4.18}$$

τ_0 and τ_1 are used as free parameters in a fit of the simulated CCE curve. The fit was performed with the method of the least squares (see Figure 4.11).

The root mean square deviation (RMS Deviation) between simulation and data was calculated by

$$\text{RMS Deviation} = \sqrt{\frac{\sum_{i=1}^{n}(CCE_{sim} - CCE_{data})^2}{n}}. \tag{4.19}$$

It turns out that the data can be described best when using a trapping time which is linearly dependent on the electric field E as described in Equation 4.16. Using other parameterisations will give greater RMSD values (see Figure 4.12).

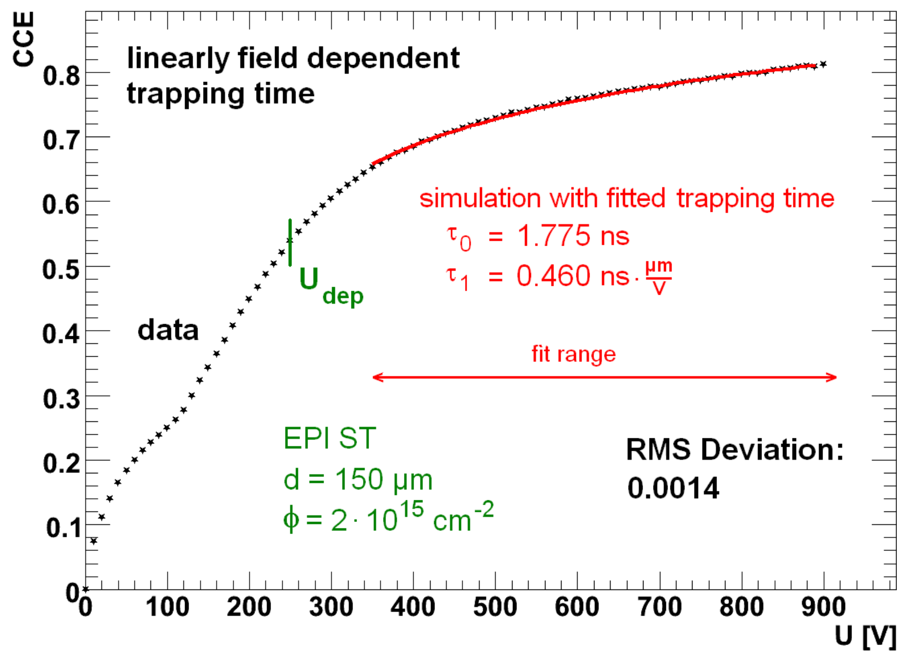

Figure 4.11: Determination of the trapping time using a CCE fit.

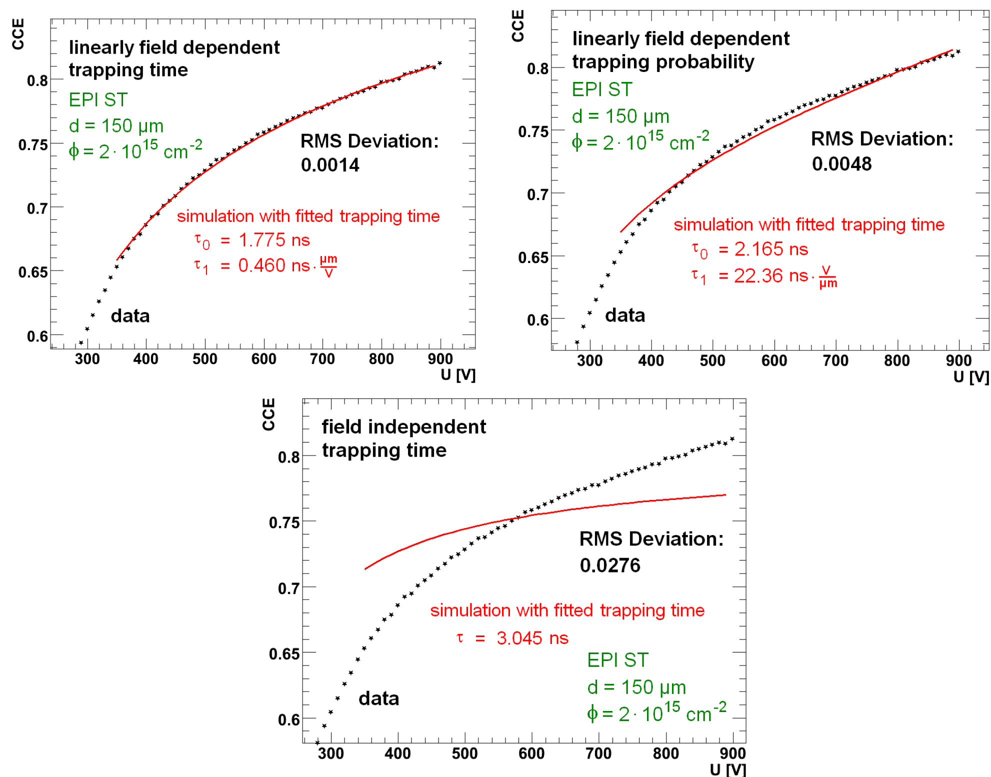

Figure 4.12: Comparison of different trapping time parameterisations. With a field independent trapping time the data is not described. Linearly field dependent trapping time fits the data best giving the lowest RMS deviations.

The data could also be described well when assuming a linearly voltage dependent trapping time, but as already seen in Section 2.4.4 there is some motivation to consider trapping to be dependent on the local electric field. For the following analysis we will perform all fits assuming a linearly field dependent trapping time according to Equation 4.16.

The RMSD values are smaller than 0.002 (or ~ 0.3 % in Q_0)[3] for most measurements if a linear field dependent trapping time is assumed. The uncertainty in Q_0 due to instabilities in the setup is taken into account with 1 % and hence it is large compared to the RMSD. We conclude that the simulated CCE curve can be fitted to the data very precisely compared to systematic errors which need to be taken into account. The greatest contributions are given by uncertainties in the amount of deposited charge Q_0 and by uncertainties in the diode thickness d.

If uncertainties of d are taken into account with 2 µm (compare Table 5.1) this leads to variations of the fit results in the order of 2 %. Uncertainties of the deposited charge Q_0 are taken into account with 1 % leading to errors of the fit results in the order of 5 % (more for neutron fluences $< 10^{15}$ cm^{-2}).

The uncertainties of the space charge distribution N_{eff} lead to uncertainties in the electric field and hence in the drift velocity which then affects the fit results. However, the effect on the fit results is small for two reasons. For voltages much higher than the full depletion voltage the drift velocity is close to the saturation velocity and hence the charge collection hardly depends on the space charge distribution. For lower voltages of the fit range in the order of 100 Volts above full depletion, charge collection is described very precisely by extracting the space charge distribution from the TCT current signal as explained below.

4.4.4 Determination of the Space Charge Distribution

While for unirradiated diodes a homogeneous space charge distribution and a linear electric field is present and the TCT current signal can be described well, in highly irradiated silicon TCT current signals with a double peak structure are observed. Figure 4.13 shows that these TCT current signals can not be described assuming a homogeneous space charge. In order to describe these observed double peak structures non-linear electric fields and hence inhomogeneous space charge distributions needs to be assumed. The first order correction to homogeneous space charge would be to consider linearly distributed space charge resulting in parabolic electric fields. This way the observed double peaks could be successfully described (compare Figure 4.14).

For the shown diode (Figure 4.13 and Figure 4.14) with a neutron fluence of $\phi = 2\cdot 10^{15}$ cm^{-2} the results of the CCE fit differ by about 10 % in τ_1, while $\tau(E)$ differs by only up to 5 % for the investigated electric field regime[4] (compare Figure 4.15). We may assume that for low fluences in the order of 10^{14} cm^{-2} the difference between both cases is much smaller and

[3] The CCE data is calculated by $CCE = Q/Q_0$. For $CCE \approx 0.7$ a deviation of 0.002 is ~ 0.3 % in Q_0.

[4] Measurements were performed up to 1000 V max.. The average field strength for the 150 µm thick diode at 1000 V is $E \approx 7$ V/µm.

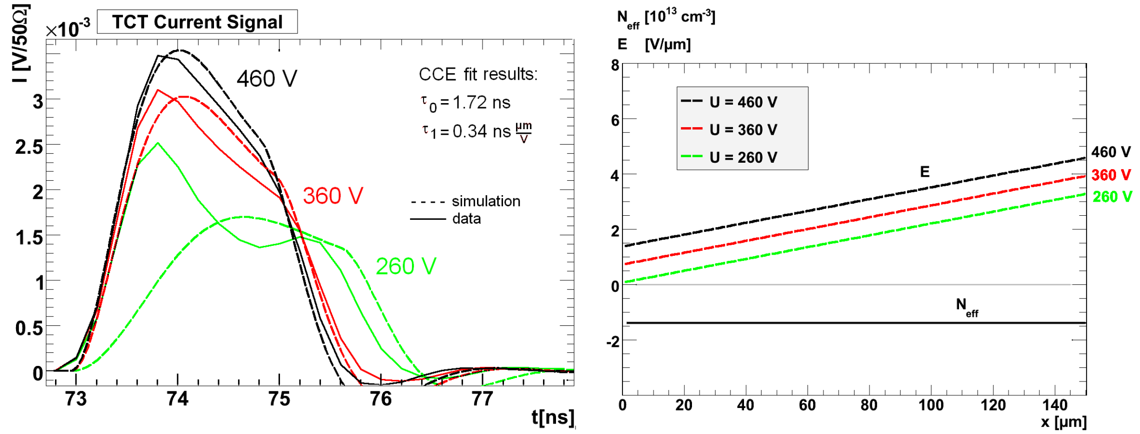

Figure 4.13: TCT current signal simulated with homogeneous space charge and linear electric field for the 150 µm EPI-DO diode with $\phi = 2 \cdot 10^{15}$ cm^{-2}. Especially at voltages close to $U_{dep} = 250$ V the approximation of a homogeneous space charge extracted from CV measurements does not describe the signal.

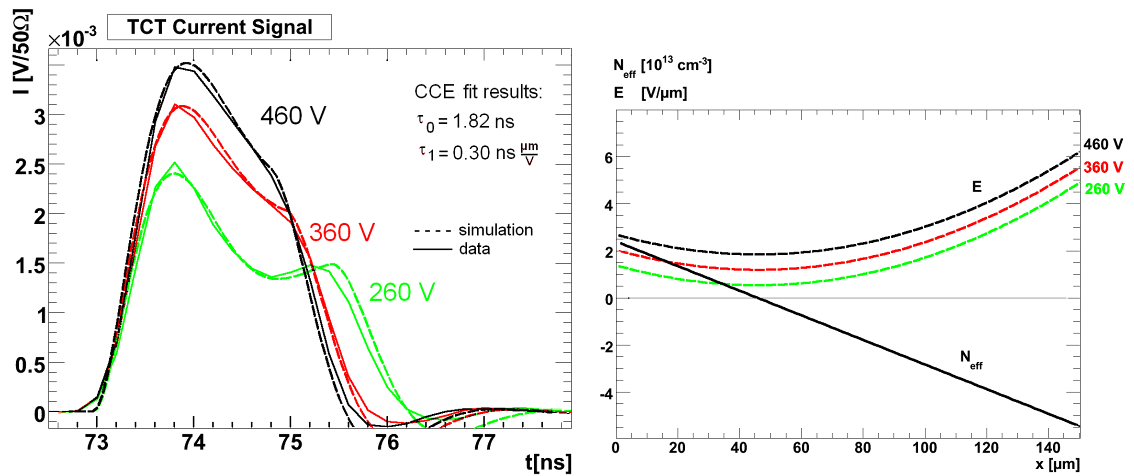

Figure 4.14: TCT current signal simulated with a linear space charge distribution and parabolic electric fields describes the 150 µm EPI-DO diode with $\phi = 2 \cdot 10^{15}$ cm^{-2} better compared to a homogeneous space charge distribution.

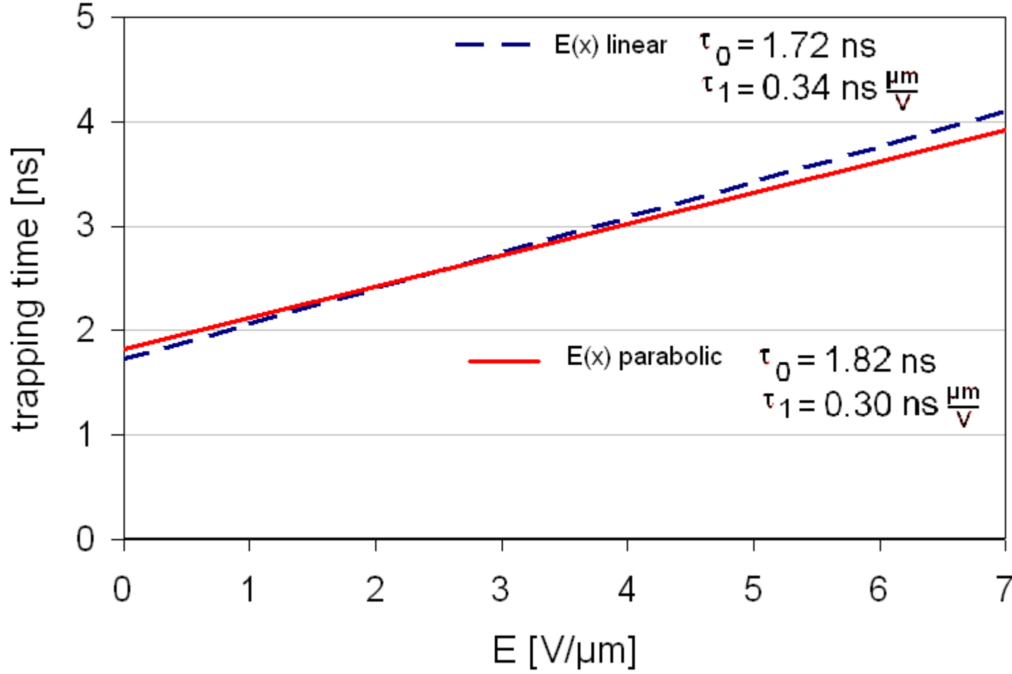

Figure 4.15: Trapping time versus electric field for different space charge distributions assumed for the 150 μm EPI-DO diode with $\phi = 2 \cdot 10^{15}$ cm^{-2}.

we may assume linear electric fields there. This approximation is necessary because for the low fluences we have only big diodes available. The higher capacitance degrades the time resolution and the space charge distribution can not be extracted from the TCT current signal as explained below, but only from CV measurements.

The linear space charge distribution $N_{eff}(x)$ is parameterised using the average space charge of the diode, $\bar{N}_{eff}$, and the inhomogeneity of space charge ΔN_{eff}, which we define as the difference between $\bar{N}_{eff}$ and the extremum of $N_{eff}(x)$ as following:

$$N_{eff}(x) = \bar{N}_{eff} + \left(1 - \frac{x}{d/2}\right) \Delta N_{eff} \tag{4.20}$$

Also compare Figure 4.16. In this parameterisation a homogeneous space charge distribution refers to $\Delta N_{eff} = 0$ and hence $N_{eff}(x) = \bar{N}_{eff}$.

In order to extract the space charge distribution from the TCT current signal, we try different values for $\bar{N}_{eff}$ and ΔN_{eff} until the TCT current signal is described well as seen in Figure 4.14. This procedure can be performed at different voltages. For voltages very close or below U_{dep} the parameters $\bar{N}_{eff}$ and ΔN_{eff} turned out to be very sensitive on the voltage chosen. This is expected for not fully depleted diodes because the depletion width and hence the space charge at the depletion junction changes with voltage. E.g. donor states in the undepleted region release their electron when they are depleted by increasing the voltage and then have positive contribution to the local space charge density.

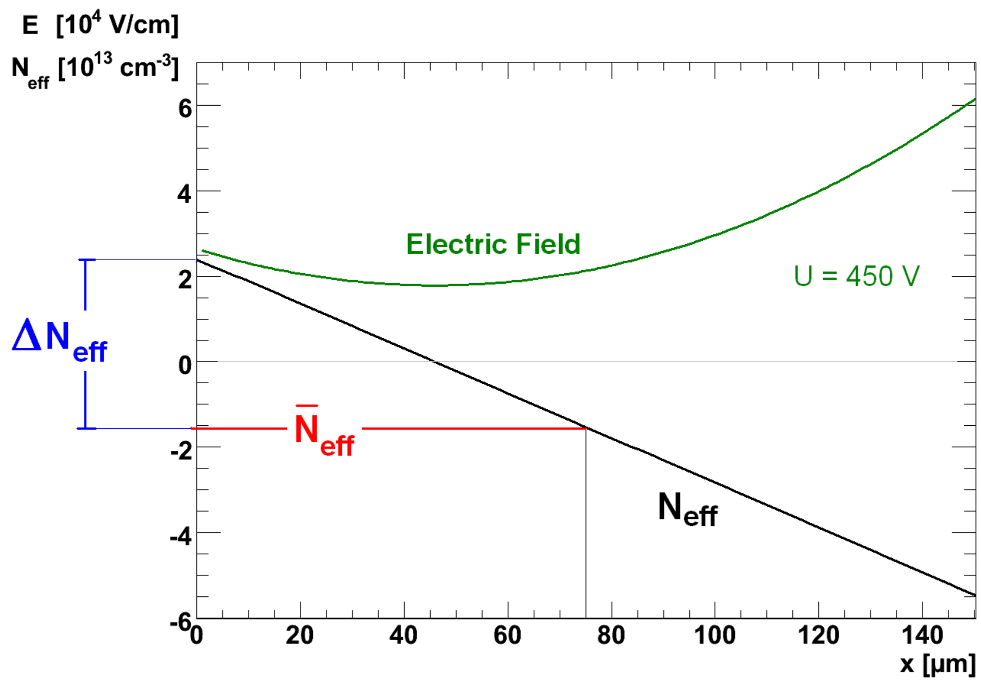

Figure 4.16: Parameterisation of the space charge distribution according to Equation 4.20 with $\bar{N}_{eff} = -1.6 \cdot 10^{13}$ cm^{-3} and $\Delta\ N_{eff} = 4 \cdot 10^{13}$ cm^{-3} and its parabolic electric field E. The values correspond to the 150 µm EPI-DO diode with $\phi = 10^{15}$ cm^{-2}.

For voltages 50 Volts and more above U_{dep} the parameters were more stable and nearly independent of the voltage chosen. Sometimes higher values for $\bar{N}_{eff}$ and ΔN_{eff} were needed in order to describe the data at higher voltages better. In this case we allow $\bar{N}_{eff}$ and ΔN_{eff} to be linearly dependent on the applied voltage as following:

$$\bar{N}_{eff} = \bar{N}_{eff,0} + \bar{N}_{eff,p} \cdot \frac{U}{100\text{V}}, \qquad \Delta\ N_{eff} = \Delta\ N_{eff,0} + \Delta\ N_{eff,p} \cdot \frac{U}{100\text{V}} \tag{4.21}$$

For all examined diodes the change of $\bar{N}_{eff}$ and ΔN_{eff} when U was changed by 100 V was between 0 % and 5 % in order to describe the TCT current signals best. The TCT current signal is sensitive to the space charge distribution only if small electric fields are present and in our case up to a couple of 100 Volts above full depletion voltage.

Hence we did not investigate the voltage dependency of N_{eff} further. In order to have reproducible results all presented data concerning the space charge will be extracted at 100 V above U_{dep}.

Chapter 5

Results and Discussion

In the following section the results obtained from the CV-IV curves and from the measured TCT signals will be presented. The TCT signals were analysed using either the charge correction method (CCM) or the simulation of charge collection.

The behaviour of the CCM results turned out to contradict important CCM assumptions. Hence more emphasis on the simulation of charge collection was put. The simulation was used to determine both, the information on the space charge distribution and on the trapping time.

5.1 CV-IV Measurements

The results obtained from CV-IV measurements are presented in Table 5.1 and will be discussed below.

5.1.1 Annealing Studies and Type Inversion

The irradiated diodes with neutron fluences $\phi > 2\cdot 10^{14}$ cm^{-2} show a decrease of the depletion voltage during short term annealing. As discussed before in the case of neutron irradiation this behaviour corresponds to a negative space charge. Hence the diodes with $\phi > 2 \cdot 10^{14}$ cm^{-2}, which had a positive space charge before, are type inverted (compare Figure 5.1).

Diodes of the same type (n-type EPI-DO and EPI-ST) were investigated after proton irradiation by [Lan08]. No type inversion was observed, i.e. the space charge was still positive after irradiation. This effect is also seen in the microscopic studies. After proton irradiation a high concentration of a donor-like defect called E(30K) is seen. When depleted, E(30K) gives a positive space charge overcompensating the space charge of acceptor-like defects. No space charge sign inversion takes place. For neutron irradiation the E(30K) concentration is much lower and its positive contribution to the space charge is less. It does not overcompensate the negative space charge of introduced acceptor-like defects. See [Pin09] for more details.

Diode	Fluence $[10^{15}$ cm$^{-2}]$	U_{dep} [V]	I_{dep} [µA]	$C_{end}^{unirrad}$ [pF]	d [µm]	N_{eff} $[10^{12}$ cm$^{-3}]$
261636-11-45-3	0	132	< 1	4.30	151.0	7.6
261636-11-25 (big)	0.1	51	169	17.2	150.7	3.0
261636-11-27 (big)	0.3	26	180	17.4	149.7	-1.5
261636-11-14-1	1	105	25	4.32	150.4	-6.1
261636-11-39-1	2	251	67	4.26	152.7	-14.2
261636-11-20-1	3	329	109	4.27	152.1	-18.7
261636-11-45-1	4	392	-	4.28	151.6	-22.4
261636-14-45-3	0	134	< 1	4.35	149.3	7.9
261636-14-14-1	1	115	25	4.31	150.6	-6.6
261636-14-39-1	2	252	62	4.24	153.4	-14.1
261636-14-56-1	3	348	105	4.31	150.8	-20.1
261636-14-29-1	4	419	683	4.31	150.6	-24.3
261636-4-14-2	0	116	< 1	6.51	99.8	15.3
261636-4-14-1	1	40	16	6.56	99.0	-5.4
261636-4-39-1	2	99	33	6.43	101.0	-12.7
261636-4-56-1	3	136	50	6.56	99.0	-18.2
261636-4-12-1	4	171	63	6.66	97.5	-23.6

Table 5.1: Depletion voltage U_{dep}, doping concentration N_{eff}, reverse current I_{dep} and diode thickness d obtained from CV-IV measurements. I_{dep} is taken at U_{dep} and room temperature after 30 minutes annealing at 80 °C, d is calculated from $C_{end}^{unirrad}$ using the pad area $A = 6.17$ mm^2 which was measured using a microscope and $4A$ for the big diodes, and N_{eff} is calculated from U_{dep} taking into account type inversion.

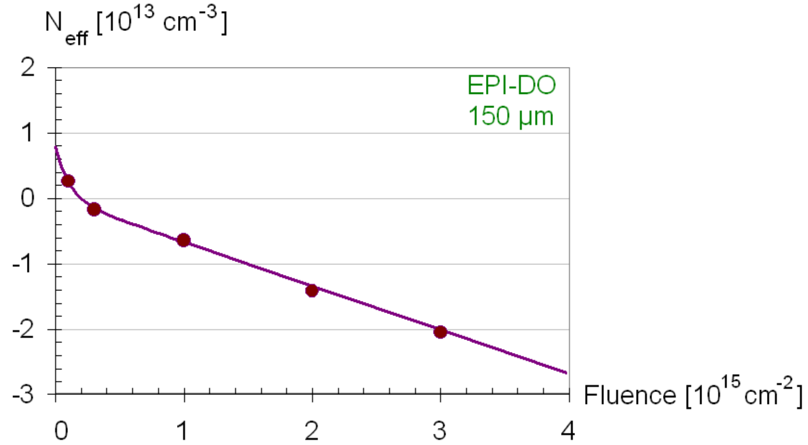

Figure 5.1: Space charge density calculated from CV measurements after 8 minutes annealing at 80 °C (10 kHz at $T = 20$ °C) and a fit by Equation 4.3.

d in µm	c in 10^{-15} cm^{-3}	g in 10^{-3} cm^{-3}	type inversion for $\phi >$	
EPI-DO, 150	8.9	6.7	$\sim 2 \cdot 10^{14}$ cm^{-2}	
EPI-DO, 72	2.1	5.5	$\sim 8 \cdot 10^{14}$ cm^{-2}	by [Koc07]
EPI-ST, 72	2.0	4.9	$\sim 8 \cdot 10^{14}$ cm^{-2}	by [Koc07]
EPI-ST, 50		-5	no inversion	by [Lin06b]

Table 5.2: Donor removal constant c and effective introduction rate g for EPI-DO diodes of different thicknesses for neutron irradiation.

5.1.2 Depletion Voltage and Space Charge Distribution

The depletion voltage U_{dep} is extracted from the CV curve for each diode as explained in Section 4.1.2. For the approximation of a homogeneous space charge distribution and an abrupt p-n junction the space charge density N_{eff} was calculated using Equation 2.5. The space charge density calculated from CV measurements as a function of neutron fluences ϕ is shown in Figure 5.1. The shown fit corresponds to Equation 4.3 with the removal constant $c = 8.9 \cdot 10^{-15}$ cm^2 and the effective introduction rate $g = 6.7 \cdot 10^{-3}$ cm^{-1}. Values are compared with earlier investigation of epitaxial diodes after neutron irradiation by [Koc07] and [Lin06b] in Table 5.2. For thinner diodes we find a reduced effective (acceptor) introduction rate g, possibly due to a higher concentration of a donor defect in thinner diodes. A possible candidate would be the BD complex which has a higher concentration in thinner diodes after proton irradiation. See [Lin06b] for more details.

5.1.3 Radiation Induced Reverse Current I_{dep}

Before irradiation the reverse currents are much smaller than after irradiation. We determine the radiation-induced reverse current I_{dep} at the full depletion voltage U_{dep} after 30 minutes annealing at 80 °C. For most investigated diodes I_{dep} is in agreement with the expected values calculated with the damage parameter $\alpha = 3.2 \cdot 10^{-17}$ A/cm according to [Mol99] assuming

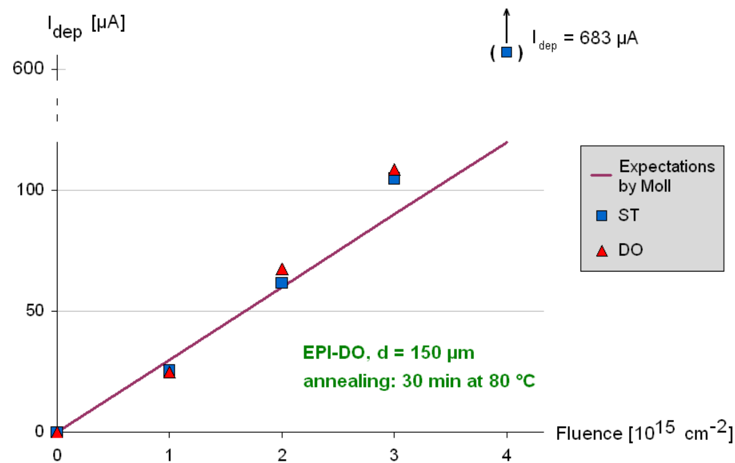

Figure 5.2: Reverse current at full depletion compared to expectations.

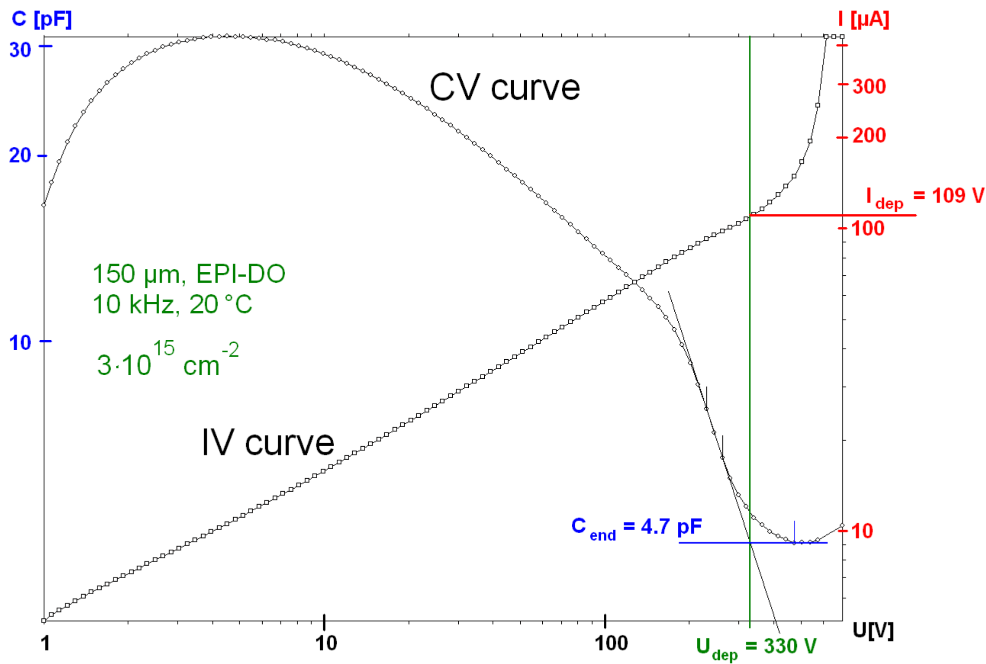

Figure 5.3: CV and IV curve for an irradiated diode with $\phi = 3 \cdot 10^{15}$ cm^{-2}. Increased reverse currents at voltages above U_{dep} are seen.

a fluence uncertainty of 10 percent.

However, for some diodes an increase of reverse current is found. I_{dep} for the small 150 µm diodes is shown in Figure 5.2. The value for the EPI-ST diode with a neutron fluence of 4 $\cdot$ 10^{15} cm^{-2} is much higher than expected. Already at fluences of $3 \cdot 10^{15}$ cm^{-2} we see slightly higher reverse currents compared to expectations. In Figure 5.3 the IV curve for the EPI-DO diode with $\phi = 3 \cdot 10^{15}$ cm^{-2} is shown. An exponential increase of reverse current is seen for voltages above full depletion. Possibly the slightly higher reverse current at the full depletion voltage is caused by charge multiplication.

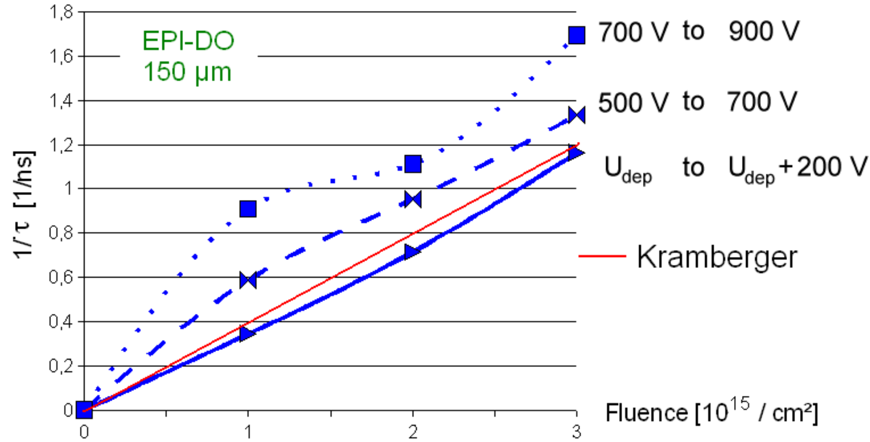

Figure 5.4: Trapping probability extracted from the CCM. Different voltage ranges for the zero-slope condition were used. Shown are measurements of the 150 µm EPI-DO diodes compared to extrapolations of the results by [Kra01] ($\beta = 4 \cdot 10^{-16}$ cm^2/ns).

5.2 Charge Correction Method

In this section the results obtained with the charge correction method (CCM) and their reliability will be discussed.

5.2.1 Voltage Range for the Zero-Slope Condition

The effective trapping time τ_{eff} was calculated using the zero-slope condition as explained in Section 4.2. It is an important assumption that after trapping correction the collected charge Q_c versus bias voltage is flat above full depletion. The results obtained for τ_{eff} then should be independent of the voltage range chosen for the zero-slope condition.

It turned out that contrary to the CCM assumptions the Q_c curves are not flat above depletion. Instead a u-shape as shown in Figure 5.5 is seen, if the zero-slope condition is used. This behaviour causes the resulting τ_{eff} to depend on the voltage range chosen in which the linear fit of the $Q_c(U)$-curve is demanded to have zero slope. Figure 5.4 shows that the results obtained with the CCM are highly dependent on the voltage range chosen for the zero-slope condition.

5.2.2 Field Dependent Trapping as a Reason for Voltage Dependency

As seen before trapping cannot be corrected for by a field independent trapping time τ, giving a flat Q_c-curve when the zero-slope condition is used, and the results depend on the voltage range chosen. This behaviour indicates that at least one of the CCM assumptions is not valid.

A possible reason might be a field dependent trapping time $\tau(E)$ with larger trapping times for high electric fields as already discussed in Section 2.4.4. In this case higher applied voltages U ($U = \int E \, \mathrm{d}x$) result in larger trapping times τ. Trapping might be approximated

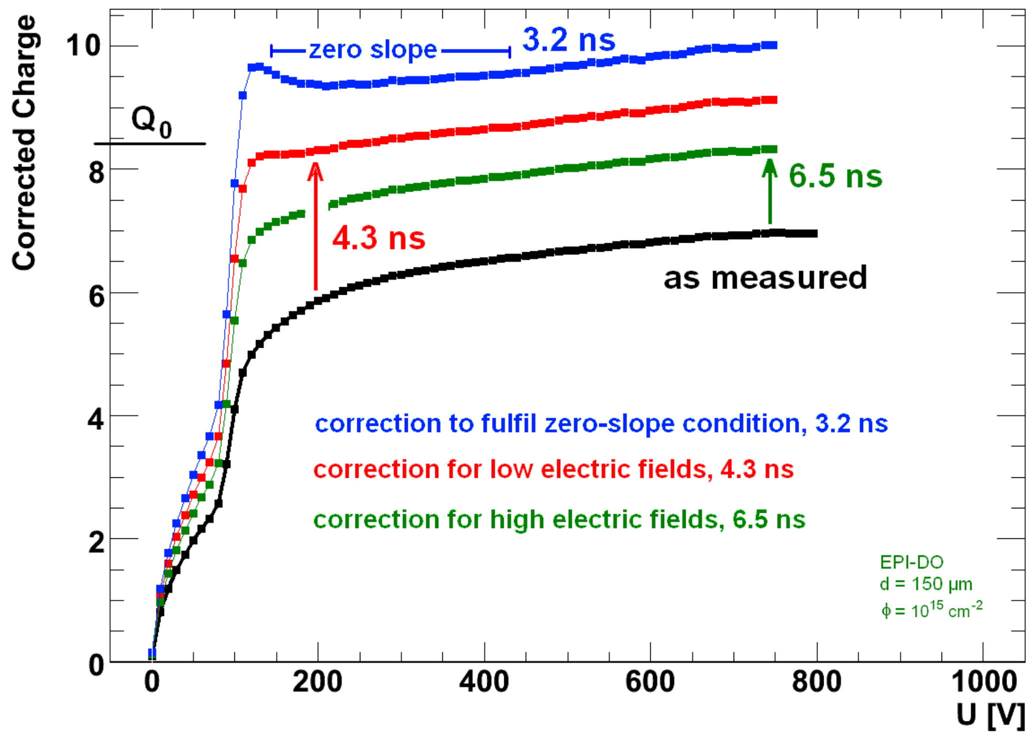

Figure 5.5: Corrected charge for different trapping times τ_{tr} for the 150 µm thick EPI-DO diode with $\phi = 10^{15}$ cm^{-2}. $\tau_{tr} = 4.3$ ns corresponds to trapping at low electric fields which are present at 200 V, $\tau_{tr} = 6.5$ ns corresponds to trapping at high electric fields which are present at 750 V. In order to fulfil the zero-slope condition τ_{tr} needs to be chosen smaller than 4.3 ns and a u-shape is seen. This corresponds to an overcorrection of trapping resulting in $Q_c > Q_0$. Q_0 is taken by comparing the Q-curve as measured with later CCE measurements at the TCT setup 4.

by a voltage dependent trapping time $\bar{\tau}(U)$ which can be calculated as a simple approximation by $\bar{\tau}(U) \approx \tau(E = U/d)$.

In order to compensate trapping we then need to correct the TCT current signal with different values of the trapping correction time τ_{tr}. A smaller one for low voltages and a larger one at high voltages. Figure 5.5 shows the trapping corrected charge for different values of τ_{tr}. The used values are taken from the simulation of charge collection and correspond to low fields in the order of 200 V/d and high fields in the order of 750 V/d.

5.2.3 Charge Carrier Density Effects

Since for the CCM no knowledge on the drift velocity and thus neither on the electric field is needed, the CCM is also applicable for very high charge carrier densities.

Larger values of τ_{eff} are found, when the charge carrier density is large compared to the doping concentration[1]. Higher trapping times in high charge carrier densities were also observed by [Bea99] and might be explained by trap filling. However, we saw above that at least one CCM assumption is not fulfilled. So no further investigations of the trapping behaviour for very high charge carrier densities were performed.

5.2.4 Time Resolution

The time resolution of the measured current pulses is characterised by 600 ps rise time at the MTCT setup. Compared to charge collection times in the order of 2 ns smearing effects might have some impact on the results and it is not clear whether the trapping correction works as assumed. The CCM assumption that effects of the electronic circuit can be neglected might be wrong in our case.

5.3 Simulation of Charge Collection

In this section the results obtained with the simulation of charge collection will be presented.

5.3.1 Space Charge Distribution

As discussed in Section 4.4.4 a linear space charge distribution was assumed and it was parameterised according to Equation 4.20 with its average value $\bar{N}_{eff}$ and its inhomogeneity[2] ΔN_{eff}. $\bar{N}_{eff}$ and ΔN_{eff} were determined by comparing the simulated TCT current signal with the measured one. This way the observed double peak structure in the TCT current signals of irradiated diodes could be described.

The results are presented in Table 5.3 and will be discussed below.

[1] We compare to the low density case and keep the voltage range for the zero-slope condition constant.

[2] We defined the inhomogeneity to be the difference between the maximal value of space charge and the average value of space charge: $\Delta N_{eff} = N_{eff}^{max} - \bar{N}_{eff}$

	Fluence ϕ [10^{15} cm^{-2}]	N_{eff} from CV [10^{12} cm^{-3}]	$\bar{N}_{eff}$ at 20 °C [10^{12} cm^{-3}]	$\bar{N}_{eff}$ at -10 °C [10^{12} cm^{-3}]	$\bar{N}_{eff}$ at -40 °C [10^{12} cm^{-3}]	ΔN_{eff} at 20 °C [10^{12} cm^{-3}]	ΔN_{eff} at -10 °C [10^{12} cm^{-3}]	ΔN_{eff} at -40 °C [10^{12} cm^{-3}]
EPI-DO	1	-6	-8	-10	-11	10	12	8
150 µm	2	-14	-16	-19	-23	40	40	35
261636-11	3	-19	-20	-22	-28	55	50	42
	4	-23	-24	-28	-30	76	70	62
EPI-DO	1	-5	-5	-5	-7	10	8	10
100 µm	2	-13	-16	-18	-22	28	32	34
261636-4	3	-18	-17	-18	-23	45	40	40
	4	-24	-22	-26	-	45	50	-
EPI-ST	2	-14	-18	-20	-24	36	32	36
150 µm	3	-20	-24	-26	-30	55	40	40
261636-14	4	-24	-29	-31	-35	60	60	50

Table 5.3: A list of space charge parameters extracted from the simulation of charge collection, compared to CV measurements at 20 °C and 10 kHz. All values are extracted at $U = U_{dep} + 100$ V with an estimated uncertainty of ±10% for $\bar{N}_{eff}$ and ±20% for ΔN_{eff}.

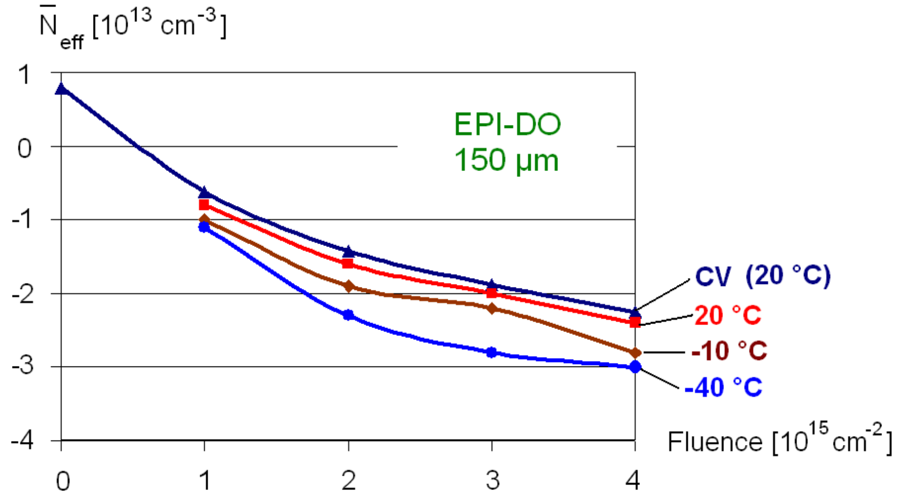

Figure 5.6: Average space charge density $\bar{N}_{eff}$ as a function of fluence for 150 µm thick EPI-DO diodes. The CV measurements were performed at room temperature at 10 kHz. TCT measurements were performed at different temperatures.

Dependence on Fluence

The results for the 150 µm EPI-DO diodes are presented in Figure 5.6 and 5.7. The obtained values of $\bar{N}_{eff}$ at different temperatures (20 °C, -10 °C,-40 °C) together with the results obtained from the CV measurements are shown in Figure 5.6. Good agreement of the $\bar{N}_{eff}$ values extracted from CV measurements and from TCT measurements are found at room temperature.

The inhomogeneity of space charge ΔN_{eff} shows greater values for larger fluences. This is expected if we assume ΔN_{eff} to be caused by the reverse current and by trapped charge carriers of the reverse current as discussed in Section 2.4.6. Larger fluences correspond to greater reverse currents and to a higher concentration of trapping centres. Hence both, the concentration of free charge carriers and the trapping probability $\frac{1}{\tau}$ is increased.

The data can be described by assuming the inhomogeneity to be linearly dependent on fluence by

$$\Delta N_{eff}(T, \phi) = \gamma(T) \cdot \phi \tag{5.1}$$

with the parameter γ of the space charge inhomogeneity. γ can be determined by a linear fit (see Figure 5.7).

Dependence on Temperature

For lower temperatures we expect two effects: a larger detrapping time for both, electrons and holes, and less reverse current in the diode. Larger detrapping times lead to a larger inhomogeneities of space charge ΔN_{eff} because trapped electrons at the back side and trapped holes at the front side stay trapped a longer period of time. At the same time the smaller

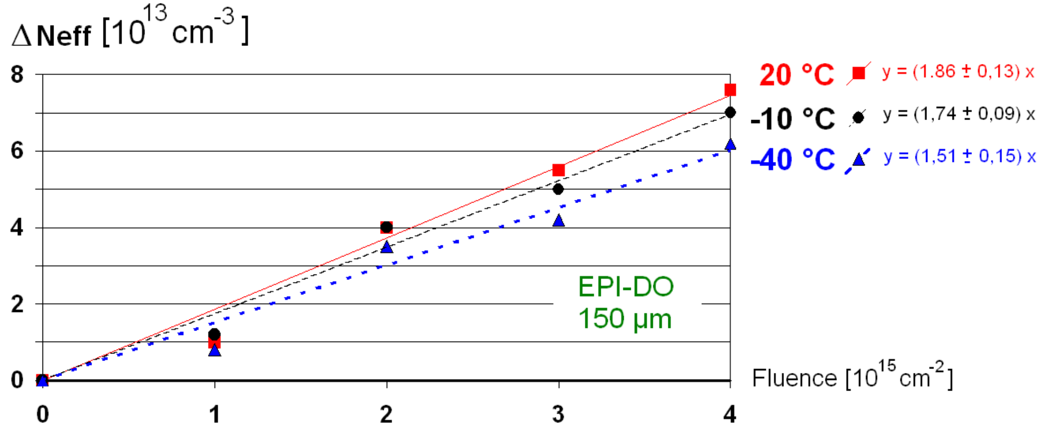

Figure 5.7: Fluence dependence of the inhomogeneity of the space charge for 150 µm thick EPI-DO diodes versus fluence.

Material	d [µm]	T [°C]	γ [10^{-2}/cm]
EPI-DO	100	-40	1.27 ± 0.27
EPI-DO	100	-10	1.31 ± 0.24
EPI-DO	100	+20	1.41 ± 0.25
EPI-DO	150	-40	1.51 ± 0.15
EPI-DO	150	-10	1.74 ± 0.09
EPI-DO	150	+20	1.86 ± 0.13
EPI-ST	150	-40	1.35 ± 0.23
EPI-ST	150	-10	1.46 ± 0.15
EPI-ST	150	+20	1.64 ± 0.10

Table 5.4: Space charge inhomogeneity parameter γ for different thicknesses, impurity concentrations and temperatures.

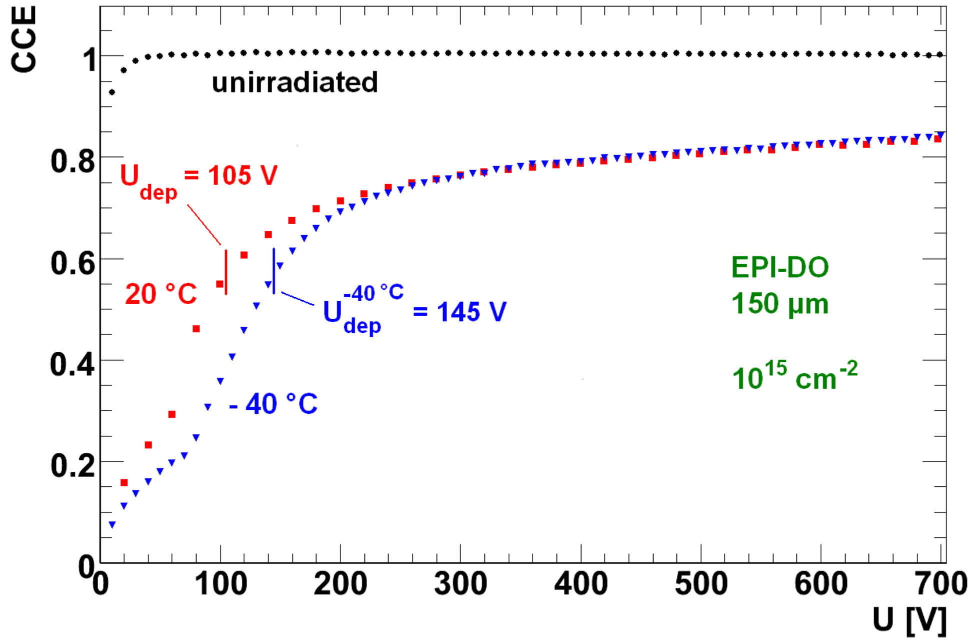

Figure 5.8: CCE curves at different temperatures for the 150 µm thick EPI-DO diode with $\phi = 10^{15}$ cm^{-2}. $U_{dep}^{-40°C}$ is calculated from $\bar{N}_{eff}$.

reverse current causes less electrons and holes to be trapped. For the 150 µm EPI-DO diodes we obtain values for the inhomogeneity parameter γ between $1.5 \cdot 10^{-2}$/cm at -40 °C and $1.9 \cdot 10^{-2}$/cm at 20 °C (see Figure 5.7 and Table 5.4). Hence the reduction of reverse current seems to have greater impact on the space charge distribution than the increase of detrapping time for lower temperatures.

The average space charge $\bar{N}_{eff}$ becomes more negative for lower temperatures (see Figure 5.6). This could be explained by a higher number of trapped electrons per unit volume due to an increased electron detrapping time. Another explanation might be a smaller number of trapped holes due to the decrease in reverse current. However, for both effects there is a counter effect of the other charge carrier type[3] and it is not clear why the counter effects should be smaller in total.

However, a smaller value of $\bar{N}_{eff}$ corresponds to a larger absolute value $|\bar{N}_{eff}|$ and hence to a higher depletion voltage U_{dep}. In Figure 5.8 one sees CCE curves with U_{dep} from CV measurements at room temperature and $U_{dep}^{-40°C}$ calculated by taking into account the change in $|\bar{N}_{eff}|$ as follows:

$$U_{dep}^{-40°C} = U_{dep} |\bar{N}_{eff}^{-40°C}| / |\bar{N}_{eff}^{20°C}|. \tag{5.2}$$

Also compare Equation 2.5. It can be seen that the shapes of the $CCE(U)$-curves at different temperatures agree well with the change in $|\bar{N}_{eff}|$.

[3]The hole detrapping time increases, and less reverse current causes less electrons to be trapped.

Fluence [10^{15} cm^{-2}]		T [°C]	τ_0 [ns]	τ_1 [ns µm/V]
EPI-DO	0.1	20	28	21
150 µm	0.3	20	12	3.3
	1	20	3.26	0.70
	1	-10	2.96	0.86
	1	-40	2.57	1.04
	2	20	1.82	0.30
	2	-10	1.58	0.42
	2	-40	1.40	0.48
	3	20	1.30	0.30
	3	-10	1.10	0.36
	3	-40	1.01	0.42
	4	20	0.82	0.34
	4	-10	0.85	0.32
	4	-40	0.76	0.32
EPI-DO	1	20	3.52	0.16
100 µm	1	-10	3.40	0.22
	1	-40	3.10	0.26
	2	20	1.90	0.30
	2	-10	1.71	0.32
	2	-40	1.61	0.32
	3	20	1.28	0.20
	3	-10	1.10	0.23
	3	-40	1.01	0.21
	4	20	0.89	0.28
	4	-10	0.98	0.28
	4	-40	0.69	0.50
EPI-ST	2	20	1.78	0.46
150 µm	2	-10	1.77	0.46
	2	-40	1.38	0.58
	3	20	1.40	0.33
	3	-10	1.29	0.38
	3	-40	1.13	0.44
	4	20	0.86	0.42
	4	-10	0.85	0.38
	4	-40	0.59	0.54

Table 5.5: List of trapping times obtained from the simulation of charge collection.

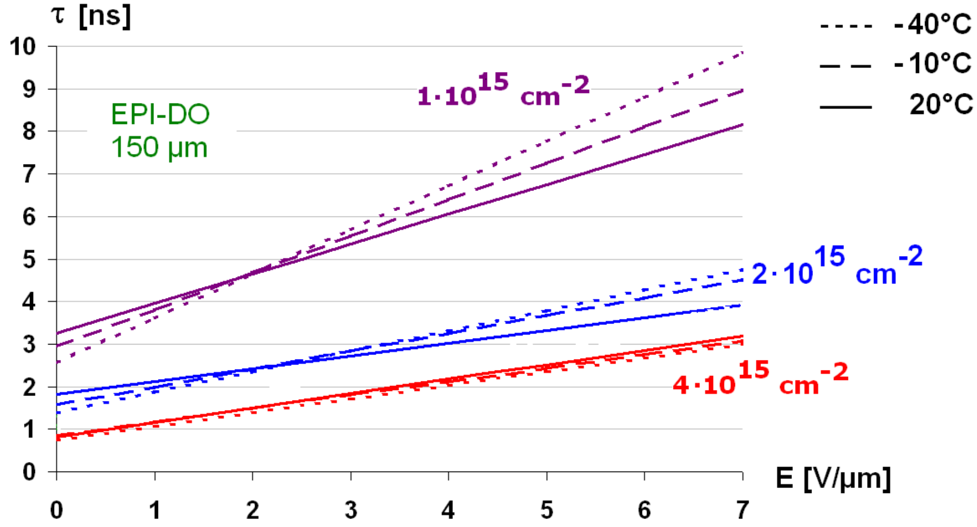

Figure 5.9: Trapping time versus electric field at different temperatures and fluences for the 150 µm thick EPI-DO diode.

5.3.2 Trapping Time

As already discussed in Section 4.4.3 the measured CCE curves could be described best, when assuming the trapping time to be linearly dependent on the electric field. The fit results of the trapping time are presented in Table 5.5 and for some diodes illustrated in Figure 5.9. The dependence on the electric field, on the fluence, on the temperature, on the oxygen concentration and on the diode thickness will be discussed below.

Dependence on Electric Field

As already seen in Figure 5.9 trapping time is larger for high electric fields. We define the degree of field dependence to be the normalised slope of $\tau(E)$ as follows:

$$\left(\frac{E}{\tau}\frac{\mathrm{d}\tau}{\mathrm{d}E}\right)_E = \frac{E \cdot \tau_1}{\tau(E)}. \tag{5.3}$$

At the medium strong[4] electric fields of $E = 4$ V/µm the degree of field dependence is shown in Figure 5.10. No significant dependence on fluence can be seen and we may conclude that the field dependence of trapping might be present at all fluences.

Also [Bea99] found the trapping time to depend on the applied voltage for neutron fluences of 1 to 3 $\cdot 10^{14}$ cm^{-2}. For fluences below $1 \cdot 10^{14}$ cm^{-2} no investigation on the field dependence of trapping could be found in the literature.

[4] $E = 4$ V/µm is the average field strength if 600 V are applied. 600 V were usually included in the fit range (Compare 4.11).

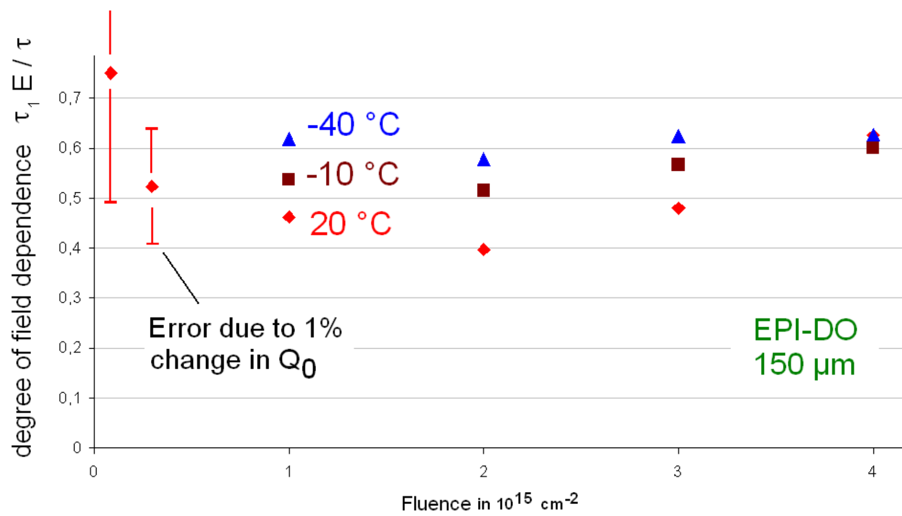

Figure 5.10: Degree of field dependence at E=4 V/µm (see Equation 5.3) versus fluence at different temperatures. 150 µm thick EPI-DO diodes were used. The uncertainty of the fit results is higher for low fluences.

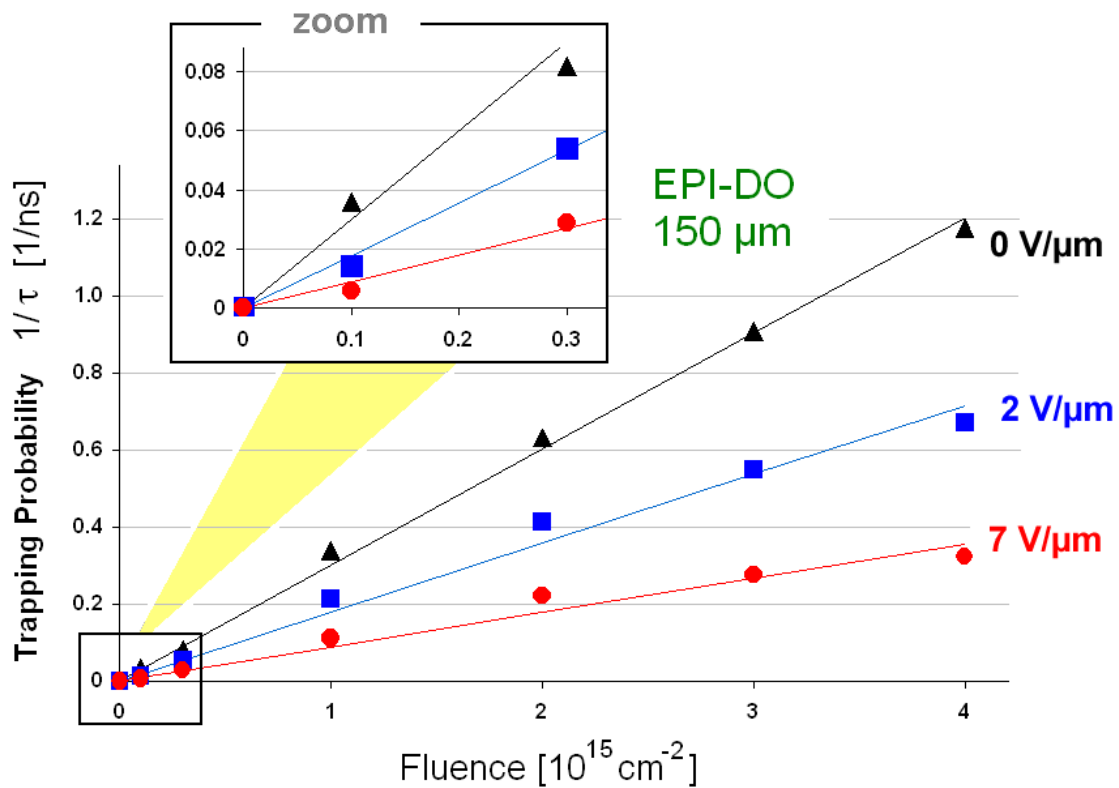

Figure 5.11: Trapping probability versus fluence for 150 µm thick EPI-DO diodes at -10 °C and different electric fields.

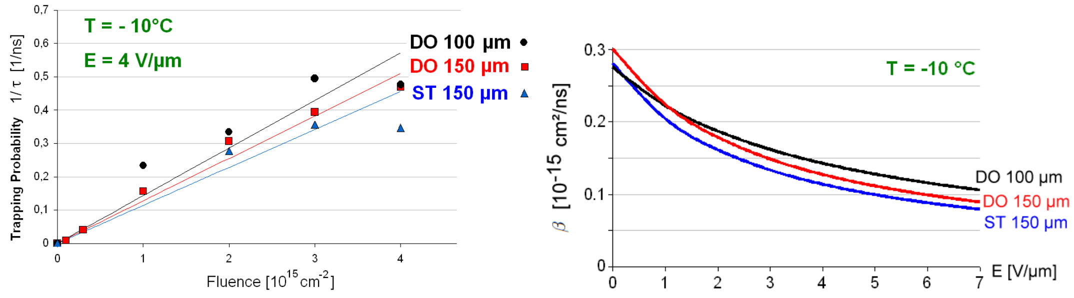

Figure 5.12: Trapping probability versus fluence at $E = 4$ V/µm (a) and β versus E (b) for EPI-DO and EPI-ST diodes of different thicknesses.

Dependence on Fluence

In previous investigations by [Kra01] the trapping time was assumed to be field independent and the trapping probability $1/\tau$ was found to be proportional to the fluence ϕ:

$$\frac{1}{\tau} = \beta\phi. \tag{5.4}$$

Figure 5.11 shows the trapping probability versus fluence for different electric fields. The trapping probability was fitted according to Equation 5.4. The fit describes the data well for low electric fields, i.e. the trapping probability is proportional to the fluence. For high electric fields the fit describes the data not as well: less trapping is seen at high fluences of $3 \cdot 10^{15}$ cm^{-2} and above compared to the linear extrapolation of the values for lower fluences.

However, the fit was performed and the β values as function of electric field are shown in Figure 5.12. Less trapping is observed compared to investigations by [Kra01], who found the proportionality factor β to be close to $4 \cdot 10^{-16}$ cm^2 ns^{-1} for electrons in neutron irradiated diodes at T = -10 °C using the charge correction method. He found smaller values of β for higher temperatures.

Dependence on Temperature

The trapping time shows a higher field dependence for lower temperatures (see Figure 5.10). For low electric fields $E \leq 1$ V/µm we have shorter trapping times (more trapping) at low temperatures (see Figure 5.9). This can be explained by shallow defects which do not contribute to the effective trapping for room temperature because detrapping is very fast, or by temperature dependent trapping cross sections σ. This effect is in agreement with the investigation by [Kra01] who also found shorter trapping times for lower temperatures and hence larger values of β.

For high electric fields there might be field enhanced very fast detrapping for shallow defects independent of temperature. This fast detrapping at high electric fields would then ionise the shallow defects and they would not contribute to the effective trapping. In this case the temperature dependence on trapping time which was seen at low electric fields would not

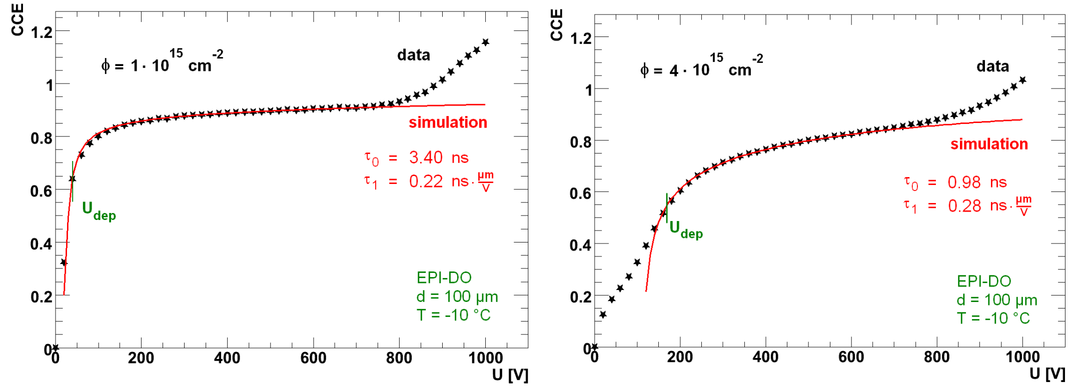

Figure 5.13: CCE curves for 100 µm EPI-DO diodes at $T = -10$ °C. Red line: simulation. Black stars: data.

be seen for high fields.

In Section 5.3.1 it was already seen that the space charge distribution is temperature dependent. Higher occupation probability of trapping centres due to increased detrapping time for lower temperatures might explain higher trapping times (less trapping) for lower temperatures.

Dependence on Oxygen Concentration and Diode Thickness

The trapping probability for medium strong fields ($E = 4$ V/µm) and the field dependence of the β value are shown in Figure 5.12 for different diode thicknesses and oxygen concentrations. No significant dependence on diode thickness and oxygen concentration could be found.

In all former investigations the trapping probability was also found to be independent of oxygen concentration and diode thickness.

5.3.3 Charge Multiplication

While the CCE curves for 150 µm thick diodes do not indicate charge multiplication up to 1000 V and can be well described by the simulation assuming a trapping time τ with a linear field dependence, the CCE curves for 100 µm diodes show a significant increase in CCE at voltages above 800 V. Even CCE > 1 is seen.

Figure 5.13 shows the CCE as measured compared to the simulation. The difference between simulation and data above $U = 800$ V is a sign of charge multiplication making also CCE > 1 possible. Charge multiplication at high voltages would also lead to an increase of the reverse current. The behaviour of the reverse current during the CCE measurements is shown in Figure 5.14. A clear increase is seen for voltages above $U = 800$ V indicating charge multiplication.

According to [Gra73] charge multiplication, in the electric field regime relevant for the measurements presented, is described by Equation 2.16. If we assume charge multiplication only to be relevant at the position of high electric fields (at the back side of the diode) we may

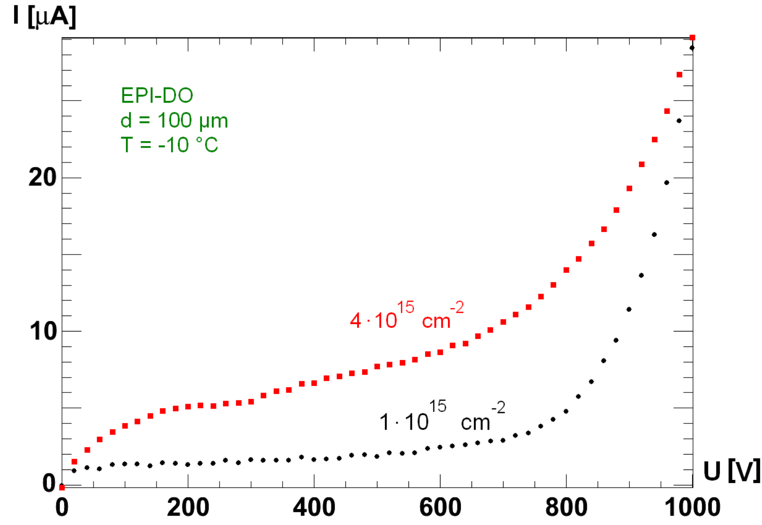

Figure 5.14: Reverse current I for the 100 µm diodes as a function of voltage U.

simplify the problem as following: we only consider charge multiplication in the last 10 µm of the diode (compare Figure 5.15) and assume a homogeneous electric field there. As seen in Figure 2.7 in this case charge multiplication becomes relevant for electric fields in the order of $15 \cdot 10^4$ V/cm.[5]

This is larger than the electric field seen in Figure 5.15 which is in the order of $13 \cdot 10^4$ V/cm and corresponds to $U = 1000$ V and to the space charge distribution $N_{eff}(x)$ which was found at depletion voltage[6].

It might be that the space charge distribution at high voltages is changed in such a way that we have higher electric fields at the back side of the diode compared to the fields which we get when assuming N_{eff} to be independent of voltage. In this case we would need either larger values of $|\bar{N}_{eff}|$ or larger values of ΔN_{eff} at higher voltages.

Another reason why we see charge multiplication can be due to defects in the silicon bulk causing locally very high electric fields. Charge multiplication may then take place only close to these defects. In this case a linear distribution of space charge as used in the simulation would not be able to describe charge multiplication effects quantitatively.

[5]For this fields we have a charge multiplication factor of ~ 1.1. About 50 % of the electrons (more for low fluences) reach the back side of the diode and deposit new charge there (electrons and holes). Hence we would expect an increase in CCE by about 5%.

[6]For the 100 µm thick diodes time resolution was not sufficient to extract the space charge at high voltages. Time resolved TCT current signals were only achieved close to the voltage of full depletion.

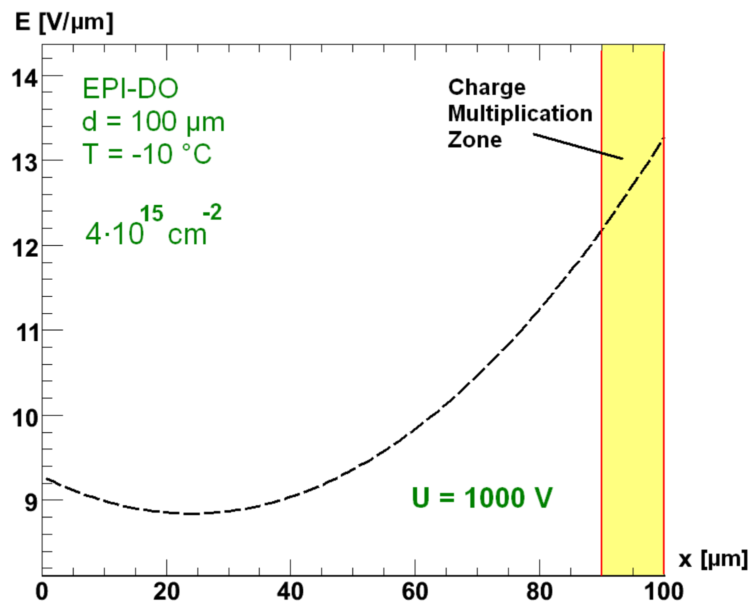

Figure 5.15: Electric field and charge multiplication zone in a 100 µm thick diode at $T = -10\,°\mathrm{C}$ and $U = 1000$ V. Charge multiplication may be assumed only to be relevant only at high electric fields at the back side of the diode.

Chapter 6

Summary and Conclusion

The aim of this work was the investigation of the charge collection in neutron irradiated silicon sensors with an emphasis on the trapping behaviour and on the space charge distribution. Epitaxial p^+n-silicon pad diodes of different thicknesses (100 µm and 150 µm) and impurity concentrations (standard and oxygen enriched epitaxial silicon) were irradiated with neutrons fluences up to $4 \cdot 10^{15}$ cm^{-2}. These fluences will occur in the inner pixel layers close to the interaction point at the SLHC experiments after 5 years of operation.

By improving the stability of the TCT-system and making measurements of unirradiated diodes before and after the measurements of irradiated diodes, the simultaneous measurement of the absolute charge collection efficiency and of the time resolved current signals with a rise time of 650 ps for 150 µm thick silicon diodes has been achieved for the first time.

A new cooling system allows measurements down to -40 °C.

The main results obtained in this work are summarised in the following.

Results

It has been shown that the standard charge correction method (CCM) cannot be used to determine the trapping times in thin irradiated silicon sensors. The charge collection times are too short compared to the rise time of the system and the assumption of field independent trapping is not valid. Thus a new analysis method has been developed which calculates the current pulses for an inhomogeneous space charge distribution and for a field dependent electron trapping time. The results are compared to the measured TCT current signals to determine the space charge distribution in the diode and the field dependent trapping time. It is found that the data can be described with a linear space charge distribution resulting in a double peak structure in the TCT current.

The average space charge density $\bar{N}_{eff}$ determined from the TCT measurements showed good agreement with the space charge density extracted from standard CV measurements at room temperature. For all investigated diodes with neutron fluences greater than $2 \cdot 10^{14}$ cm^{-2} type inversion was observed. For smaller temperatures higher values of $|\bar{N}_{eff}|$ were found.

The inhomogeneity of the space charge ΔN_{eff} was found to increase with fluence and

decrease with temperature. Both effects agree with the assumption that the change of charge state of the radiation induced traps due to the reverse current is responsible for the inhomogeneity of the space charge.

The charge collection efficiency determined in TCT measurements could be described with a linearly field dependent trapping time τ. The field dependence of trapping turned out to be relevant at all investigated fluences. τ increases by a factor of two for electric fields between 1 V/µm and 6 V/µm.

Higher values of τ were observed compared to previous investigations with the charge correction method and the assumption of a field independent trapping time. The trapping probability $1/\tau$ was found to be proportional to fluence. It is not clear whether this description still holds at high electric fields and high fluences.

Charge collection efficiencies greater than 1 were found for 100 µm thick diodes at voltages above 800 V and indicate charge multiplication.

Conclusions

This study of neutron-irradiated epitaxial silicon detectors complements a study of proton-irradiated epitaxial silicon detectors, both at SLHC fluences. Type inversion of n-type silicon was found for neutron irradiation but not for proton irradiation.

At the SLHC there will be a mixed irradiation with charged and neutral hadrons. Similar studies with different silicon materials and mixed irradiations will be performed in the frame of the Central European Consortium[1] with the aim to find a single material and module design for the outer tracker of the SLHC experiments.

Thin silicon diodes are a promising option for the SLHC experiments because short charge collection times and high electric fields decrease the influence of trapping and high electric fields might lead to charge multiplication.

[1] The Central European Consortium (CEC) is a collaboration of 9 institutes. [Die09]

List of Figures

1.1 Super LHC equivalent fluences, normalised to 1 MeV neutrons. By [Mol99]. 2

2.1 Oxygen concentration depth profile in 100 µm and 150 µm EPI diodes. Measurements were performed by SIMS and illustrated by [Lan08]. 4
2.2 The p-n junction. 5
2.3 Fully depleted p-n junction. 6
2.4 CV and IV curve for an unirradiated EPI-DO diode with a thickness of 150 µm, measured at 20 °C with 10 kHz frequency. 7
2.5 Principle of a silicon detector 8
2.6 Anisotropy effects of the drift velocity of electrons 9
2.7 Ionisation rate α and multiplication factor M 11
2.8 Point defects in a silicon lattice schematically 12
2.9 Reverse current in a silicon diode 15

3.1 a) Schematic top view (front side) and b) cross section of the used pad diodes by [Koc07] and [Lan08]. 18
3.2 Movement of charge carriers after electron-hole pair production on the front side. 19
3.3 The used laser TCT setups schematic. 20
3.4 Signal stability for the red laser at TCT setup 4. 22
3.5 Determination of the collected charge Q 23
3.6 Comparison of CCE curves for different shaping times at the TCT3 with the charge sensitive amplifier and offline integration for TCT3 and TCT4. 25
3.7 Charge carrier density effects on charge collection 26

4.1 Determination of the depletion voltage U_{dep} and of the saturation capacitance C_{end} for an irradiated 150 µm thick EPI-DO diode with a neutron fluence of 10^{15} cm^{-2} at 20 °C and 10 kHz. 28
4.2 U_{dep} annealing behaviour at 80 °C for a 150 µm EPI-DO diode, after neutron irradiation with a fluence of $2 \cdot 10^{15}$ cm^{-2}. 29
4.3 Raw and trapping corrected TCT current signal 31
4.4 Deconvolution of the TCT current signal 33
4.5 Determination of τ_{eff} with the zero-slope condition. 35
4.6 Zero-slope condition for the CCM 35
4.7 Calculated electric field, drift velocity and the induced current inside of an unirradiated diode. 36
4.8 Equivalent circuit of the TCT setups 37
4.9 The simulated TCT current signal with and without circuit effects compared to measurement. $t = 0$ is chosen arbitrarily. 38
4.10 Calculated electric field, drift velocity and the induced current inside of an irradiated diode. . . 39
4.11 Determination of the trapping time using a CCE fit 41
4.12 Comparison of different trapping time parameterisations. 41

4.13 TCT current signal simulated with homogeneous space charge and linear electric field. 43
4.14 TCT current signal simulated with a linear space charge distribution and parabolic electric field. 43
4.15 Trapping time versus electric field for different space charge distributions. 44
4.16 Parameterisation of the space charge distribution. 45

5.1 Space charge density calculated from CV measurements 49
5.2 Reverse current at full depletion compared to expectation 50
5.3 CV and IV curve for an irradiated diode with $\phi = 3 \cdot 10^{15}$ cm^{-2}. 50
5.4 Trapping probability extracted from the CCM at different voltage ranges 51
5.5 Corrected charge vs Voltage for different trapping times 52
5.6 Average space charge density $\bar{N}_{eff}$ as a function of fluence. 55
5.7 Fluence dependence of the inhomogeneity of the space charge 56
5.8 CCE curves at different temperatures 57
5.9 Linear field dependent trapping time 59
5.10 Degree of field dependence of the trapping time 60
5.11 Fluence dependence of trapping for different electric fields. 60
5.12 Trapping Probability for EPI-DO and EPI-ST diodes of different thicknesses. 61
5.13 CCE curves for 100 µm diodes 62
5.14 Reverse current for the 100 µm diodes 63
5.15 Electric field and charge multiplication zone 64

List of Tables

3.1 List of the diodes investigated in this work. 18

3.2 Laser stability at the MTCT setup 22

5.1 Depletion voltage, doping concentration, reverse current and diode thickness obtained from CV-IV measurements. 48

5.2 Donor removal constant c and effective introduction rate g. 49

5.3 A list of space charge parameters extracted from the simulation of charge collection, compared to CV measurements at 20 °C and 10 kHz. All values are extracted at $U = U_{dep} + 100$ V with an estimated uncertainty of ±10% for $\bar{N}_{eff}$ and ±20% for ΔN_{eff}. 54

5.4 Space charge inhomogeneity parameter γ. 56

5.5 List of trapping times obtained from the simulation of charge collection. 58

Bibliography

[Bat05] Alison G. Bates, Michael Moll. *A comparison between irradiated magnetic Czochralski silicon and float zone silicon detectors using the transient current technique.* Nuclear Instruments and Methods in Physics Research A 555 (2005), 113-124, 2005.

[Bea99] L. Beattie, T. J. Brodbeck et al. *Carrier lifetimes in heavily irradiated silicon diodes.* Nuclear Instruments and Methods in Physics Research A 421 (1999) 502-511, 1999.

[Bec10] J. Becker, R. Klanner. *Anisotropic charge carrier mobilities in bulk silicon in presence of high electric fields* Submitted to Solid-State Electronics, to be published.

[Bro00] T. J. Brodbeck, A. Chilingarov, et al. *A new method of carrier trapping time measurement.* Nuclear Instruments and Methods in Physics Research A 455 (2000), 645-655, 2000.

[Cas09] G. Casse. *Overview of the recent activities of the RD50 collaboration on radiation hardening of semiconductor detectors for the sLHC.* Nuclear Instruments and Methods in Physics Research A 598 (2009), 54-60, 2009.

[Chi02] A. Chilingarov at al. *Carrier mobilities in irradiated silicon.* Nuclear Instruments and Methods in Physics Research A 477 (2002), 287-292, 2002.

[Ere04] V. Eremin, Z. Li., S. Roe, G. Ruggiero, E. Verbitskaya. *Double peak electric field distortion in heavily irradiated silicon strip detectors.* Nuclear Instruments and Methods in Physics Research A 535 (2004), 662-631, 2004.

[Fre07] E. Fretwurst et al. *Radiation damage studies on MCz and standard and oxygen enriched epitaxial silicon devices.* Nuclear Instruments and Methods in Physics Research A 583 (2007), 58-63, 2007.

[Gar01] S. Marti i Garcia, P.P. Allport, G. Casse, A. Greenall. *A model of charge collection for irradiated p+n detectors.* Nuclear Instruments and Methods in Physics Research A 473 (2001), 128-135, 2001.

[Gra73] W. N. Grant. *Electron and hole ionization rates in epitaxial silicon at high electric fields.* Solid-State Electronics, Vol. 16, 1189-1203, 1973.

[Jac77] C. Jacoboni et al. *A review of some charge transport properties of silicon.* Solid-State Electronics, Vol. 20, 77-89, 1977.

[Jun07] A. Junkes. *Investigation of electrically active defects induced in silicon diodes after low doses of electron and neutron irradiation.* Diploma thesis, University of Hamburg, 2007.

[Koc07] K. Koch. *Strahlenhärte von epitaktischen, Floatzone und Magnetic Czochralski-Siliziumdioden nach Neutronenbestrahlung.* Diploma thesis, University of Hamburg, 2007.

[Kra01] G. Kramberger. *Signal development in irradiated silicon detectors.* Doctoral Thesis, University of Ljubljana, 2001.

[Kra05] G. Kramberger, V. Cindro, I. Dolenc, E. Fretwurst, G. Lindström, I. Mandic, M. Mikuž, M. Zavrtanik. *Charge collection properties of heavily irradiated epitaxial silicon detectors.* Nuclear Instruments and Methods in Physics Research A 554 (2005), 212-219, 2005.

[Lan08] J. Lange. *Radiation Damage in Proton-Irradiated Epitaxial Silicon Detectors*. Diploma thesis, University of Hamburg, 2008.

[Lin06] G. Lindström, E. Fretwurst, F. Hönniger, G. Kramberger, M. Möller-Ivens, I. Pintilie, A. Schramm. *Radiation tolerance of epitaxial silicon detectors at very large proton fluences*. Nuclear Instruments and Methods in Physics research, A 556 (2006), 451-458, 2006.

[Lin06b] G. Lindström, I. Dolenc, E. Fretwurst, F. Hönniger, G. Kramberger, M. Moll, E. Nossarzewska, I. Pintilie, R. Röder. *Epitaxial silicon detectors for particle tracking - Radiation tolerance at extreme hadron fluences*. Nuclear Instruments and Methods in Physics research, A 568 (2006), 66-71, 2006.

[Li95] Z. Li, V. Eremin. *Carrier drift mobility study in neutron irradiated high purity silicon*. Nuclear Instruments and Methods in Physics Research A 362 (1995), 338-343, 1995.

[Mol99] M. Moll. *Radiation Damage in Silicon Particle Detectors*. PhD Thesis, University of Hamburg, 1999.

[Pin09] I. Pintilie et al. *Radiation-induced point- and cluster-related defects with strong impact on damage properties of silicon detectors*. Nuclear Instruments and Methods in Physics Research A 611 (2009), 52-68, 2009.

[Sel00] R. Quay, C. Moglestue, V. Palakovski and S. Selberherr. *A Temperature Dependent Model for the Saturation Velocity in Semiconductor Materials*. Materials Science in Semiconductor Processing 3 (2000), 149-155, 2000

[Sze85] S. M. Sze. *Semiconductor Devices, Physics and Technology*. John Wiley & Sons, 1985.

[Die09] A. Dierlamm, A. Junkes. *Silicon Sensor Developments: Material Design and Characterisation* Terascale Detector Development Posters, 2009, available at:
https://www.terascale.de/general_information/midterm_evaluation/

[Ver02] V. Eremin, Z. Li., E. Verbitskaya. *The origin of double peak electric field distribution in heavily irradiated silicon detectors*. Nuclear Instruments and Methods in Physics Research A 476 (2002), 556-564, 2002.

Acknowledgements

I would like to thank everyone who contributed to this work.

I am grateful to Prof. Dr. Robert Klanner for supervising this work, giving trend-setting comments, and for all the revisions on given talks, posters and reports, as well as on this thesis. Also many thanks to Prof. Dr. Caren Hagner for giving the second reference.

I am very thankful to Jörn Lange for introducing me to the world of TCT measurements and root analysis, for answering questions, giving comments, helping with technical problems and discussing results. I am also much obliged to Dr. Eckhart Fretwurst who shared his great knowledge on silicon detectors and who was always interested in the results of this work.

Many thanks to Peter Buhman for his help on CV-IV measurements and for performing some of them, to Julian Becker for his help on simulations, and to the whole detector laboratory group for sharing meals and providing a great working atmosphere.

Thanks to my family and friends for supporting me, e.g. on the appearance of this thesis. Finally I want to thank the living God for creating all the beautiful effects that were investigated in this work. For Him this thesis was written.

Hiermit versichere ich, dass ich diese Arbeit selbstständig verfasst und keine anderen als die angegebenen Quellen und Hilfsmittel verwendet habe.

Mit der Ausleihe dieser Arbeit bin ich einverstanden.

Thomas Pöhlsen, Hamburg den 14. April 2010